Stabilizing platinum atoms on CeO_2 oxygen vacancies by metal-support ┳ interaction induced interface distortion: Mechanism and application

Zeyu Jiang[a,1], Meizan Jing[b,1], Xiangbo Feng[a,1], Jingchao Xiong[c], Chi He[a,d,*], Mark Douthwaite[e], Lirong Zheng[f], Weiyu Song[b], Jian Liu[b,**], Zhiguo Qu[g,**]

[a] State Key Laboratory of Multiphase Flow in Power Engineering, School of Energy and Power Engineering, Xi'an Jiaotong University, Xi'an, 710049, Shaanxi, PR China
[b] State Key Laboratory of Heavy Oil Processing, China University of Petroleum, Beijing, 102249, PR China
[c] WISDRI City Environment Protection Engineering Limited Company, Wuhan, 430205, Hubei, PR China
[d] National Engineering Laboratory for VOCs Pollution Control Material & Technology, University of Chinese Academy of Sciences, Beijing, 101408, PR China
[e] Cardiff Catalysis Institute, School of Chemistry, Cardiff University, Main Building, Park Place, Cardiff, CF10 3AT, UK
[f] Beijing Synchrotron Radiation Facility, Institute of High Energy Physics, Chinese Academy of Sciences, Beijing, 100049, PR China
[g] MOE Key Laboratory of Thermo-Fluid Science and Engineering, School of Energy and Power Engineering, Xi'an Jiaotong University, Xi'an, 710049, Shaanxi, PR China

ARTICLE INFO

Keywords:
Single-atom catalyst
Metal-support interaction
Electronic structure
Interface distortion
VOC oxidation
Intrinsic mechanism

ABSTRACT

Exploring thermally robust single atom catalysts (SACs) is of great significance. Here, we develop a universal strategy for stabilizing Pt atoms on the mono-oxygen vacancies of CeO_2 with diverse exposed facets. The sta-bilization mechanism was proposed that the formed Pt-O-Ce interface will be taken into distortion spontaneously to keep thermodynamics stable through strong metal-support interactions. The highest degree of Pt-O-Ce dis-tortion is achieved over Pt1-CeO2{100} material, which exhibits exceptional efficiency and thermal stability for oxygenated hydrocarbon removal. The enhanced adsorption capacity of O2 and methanol confirmed in the distortion interface is seen as another crucial reason for improving the stability of SACs. Methanol oxidation on Pt1-CeO2{100} obeys the L-H mechanism under relatively low temperature and then goes through to the MVK mechanism with temperature increasing. We believe that these results would bring new opportunities in the fabrication of SACs and applications of them in thermal reactions.

1. Introduction

The dispersion of isolated metal atoms on support surfaces provides a foundation for maximizing the atomic efficiency of precious metals in catalytic reactions [1,2]. For this reason, single atom catalysts (SACs) often possess unprecedented catalytic performance, a trait which in recent years has been capitalized upon and evidenced in several im-portant reactions driven by thermal, electric, and light-energy [3–5]. In light of growing concerns associated with the emission of volatile or-ganic compounds (VOCs) [6–9], several recent publications have de-monstrated the potential of using SACs for the low-temperature de-struction of VOCs [10,11]. We too, recently demonstrated that a Pt_1-Co_3O_4 SAC was exceptionally active for the destruction of oxygenated VOCs [12]. Despite the progress made, a great challenge remains; to develop thermally and chemically stable SACs, which required to be used in large scale traditional thermal reactions, such as catalytic combustion of hydrocarbons, water-gas shift and methane mineraliza-tion [13,14]. The development of thermally robust SACs that can sus-tain reductive/oxidative processes under high temperature attracts huge interest and challenge for its application [15].

Several strategies have been invoked by researchers to synthesize materials that possess these desirable properties, consisting of (i) re-ducing the loading quantity of active metal components; (ii) adding the protective species; (iii) exploiting defect vacancies or voids in sup-porting materials [16–18]. These strategies aim to enhance metal-sup-port interactions and/or prevent the aggregating tendency of isolated atoms. However, as discussed by Xiao and co-workers, the stabilizing mechanism of classical strong metal-support interaction remains elusive in the above mentioned methods [19]. As such, we consider it to be of high importance that a logical approach is implemented, to govern the

Corresponding author at: State Key Laboratory of Multiphase Flow in Power Engineering, School of Energy and Power Engineering, Xi'an Jiaotong University, Xi'an, 710049, Shaanxi, PR China.
Corresponding author at: State Key Laboratory of Heavy Oil Processing, China University of Petroleum, Beijing, 102249, PR China./MOE Key Laboratory of Thermo-Fluid Science and Engineering, School of Energy and Power Engineering, Xi'an Jiaotong University, Xi'an, 710049, Shaanxi, PR China.
E-mail addresses: chi_he@xjtu.edu.cn (C. He), liujian@cup.edu.cn (J. Liu), zgqu@xjtu.edu.cn (Z. Qu).
[1] These authors are contributed equally to this work.

appropriate selection of metal(s) and support(s) used for the synthesis of SACs, for specific applications [20,21]. Several notable studies have investigated how support-metal strong interactions (SMSIs) influence such catalysts, using both experimental and computational techniques [22]. Li and co-workers recently investigated how on-site Coulomb interactions influence the catalytic performance of Au catalysts sup-ported on several tetravalent-metal dioxides of MO_2 (M = Ti, Zr, Ce, Hf, and Th) [23]. The study confirmed that the radial contraction and low orbital energies of the 3d and 4f orbitals in these MO_2 oxides are caused by fundamental quantum primogenic effects, which is of great sig-nificance for the determination of valence state as well as charge dis-tribution of gold atoms [23]. An additional study by O`Connor et al., predicted the interaction strengths between metal atoms and oxide supports according to the smallest absolute contraction figures and selection operator regression [24]. The investigation concluded a cor-relation between binding of interfaces and readily available physical properties of supports; such as oxophilicity measured by oxide forma-tion energy, which can be measured by the oxygen vacancy formation energy. These properties can be used to screen interaction strengths between metal-support pairs, which will undoubtedly aid the designa-tion of stable SACs moving forward [25]. Varieties of approaches are available for stabilization of isolated metal atoms; CeO_2 for instance as most extensively investigated supports for the SMSI, possesses exclusive redox properties, which have their origin in the effect of quantum primogenic, making it an ideal candidate to support and stabilize single atom sites [26]. In addition, it possesses a diverse electronic structure, which can lead to exposed facets [27].

Regrettably, much of the previous work in this area has pre-dominantly focused on dissecting information on the function of the active sites; nevertheless, the properties of heterogeneous catalysts frequently depends on the synergy between supported phases and support, the extent of which, is often magnified by means of a interface limiting effect [28]. An example of this was recently presented by Bao and co-workers [29], who constructed a series of metal-oxide inter-faces, which are considered to be the active sites for CO_2 activation and CO reduction, where a synergistic effect between Au and CeO_x pro-motes the stability of key carboxyl mediate (*COOH) and thus facil-itates CO_2 electroreduction. This has been further evidenced by Murray and co-workers [30], who proposed an evident enhancement for the CO oxidation rate in ceria-based catalysts at the ceria-metal interface, for a range of group VIII metal catalysts, revealing the significance from the support. Shen and co-workers exposed the prospect of stabilizing Au nanoparticles utilizing an interfacial anchoring pattern of gold-oxide [31], which confirmed that the structuring of Au-ceria interfaces fa-cilitates the regeneration of adsorbed molecular CO and energetic oxygen species on ceria. As such, we consider that it is crucial to design a stable mono-dispersed active interface for thermo-catalytic reactions, over which the single atom sites are anchored to the defected sites through SMSIs. Despite several single atom materials having been de-veloped and utilized for the destruction of VOCs, the intrinsic me-chanism for the oxidation of VOCs and the relationship between cata-lytic performance and electronic structure have been somewhat overlooked [6–9].

The work herein, focuses on the construction of a Pt-O-Ce active interface, in which platinum atoms are stabilized on CeO_2 oxygen va-cancies. According to our experimental and theoretical investigations, this interface was confirmed to distort; a phenomenon which is fa-cilitated by SMSIs. We propose that this SMSI is compounded by che-mical bonding and relevant charge transfer at active interfacial regions. The distortion degree at the Pt-O-Ce interfaces was enhanced attri-buting to the different electron structures of CeO_2 support with diverse exposed facets. Compared with Pt_1-CeO_2{110} and Pt_1-CeO_2{111} samples, the Pt-O-Ce active interface over Pt_1-CeO_2{100} exhibits the highest intensity of distortion degree and thus catalyst possesses the exceptional catalytic efficiency and thermal stability for oxygenated hydrocarbon removal. Furthermore, the intrinsic methanol oxidation mechanism over Pt_1-CeO_2{100} material was revealed, which further assists with the identification of active sites in these materials during oxidation reactions. We hope the present study can provide funda-mental assistance in the design of novel SACs with SMSIs; to expand the application of these catalysts in this important area of research.

2. Experimental section

2.1. Preparation of single atom catalysts

The procedures for preparation of CeO_2 supports followed the pre-vious reported [32], and the details of which were displayed in Sup-plementary Material. Immediately, the abundant surface oxygen va-cancies over CeO_2 supports were constructed by reducing in the hydrogen atmosphere at 250 °C for 2.5 h. The obtained defective sup-ports were mixed with 50 mL of deionized water and stirred for 20 min. After stirring for another 30 min, a urea solution (1 M) was added when the mixture was heated up to 60 °C, which allows the slow decom-position of urea to reach the final pH of 8.5. Then, the amount of de-sired chloroplatinic acid ($H_2PtCl_6{\cdot}6H_2O$, 1.5 mg_{Pt} mL^{-1}) was added to the above solution dropwise. The mixture was aged at 60 °C for another 1.5 h under vigorous stirring. The powder samples were collected after rotary evaporation and thorough washing with deionized water. The dried sample was obtained after keeping it in vacuum overnight at 70 °C. The single atom Pt_1-CeO_2 materials were obtained by annealing in Ar at 250 °C for 2 h and in 5% H_2/Ar at 200 °C for 2 h successively.

2.2. Catalyst characterizations

N_2 sorption isotherms were measured at 77 K on a Builder SSA-6000 apparatus. XRD measurements were performed using a powder dif-fractrometer (Bruker D8 Advance) with Cu-Kα radiation. High resolu-tion transmission electron microscopy images were recorded on a JEOL JEM-F200 (Japan) microscope. The resolution HAADF-STEM images of aberration-corrected scanning transmission electron microscopy were recorded on the ARM200F (Japan) microscope. The X-ray absorption fine structure spectra were collected in the Beijing Synchrotron Radiation Facility (BSRF). X-ray photoelectron spectroscopy experi-ments were carried out on a Thermo Fisher ESCALAB Xi^+ (America) instrument with Al-Kα radiation. The electron paramagnetic resonance spectra were measured using a A300−9.5/12 (Switzerland) X-band EPR spectrometer. Positron annihilation spectrum was performed with a Trap based slow positron beam (RGM-1/APBS-2, America). ^1H magic angle spinning nuclear magnetic resonance was recorded on the AVANCE Ⅲ 400WB (Bruck, Germany). Laser Raman spectra were ob-tained on a LabRAM HR Evolutions spectrometer (Horiba, Japan) by employing an excitation wavelength of 532 nm line of Ar ion laser. Ultraviolet-visible spectroscopy absorption spectra were recorded using a PE Lambda 950 (Perkin Elmer, America). Temperature-programmed reduction/desorption and titration experiments were recorded on a PCA-1200 (Builder, China) equipped with a TCD. operando FT-IR spectra for CO/NH_3 adsorption were performed on the Bruker Tensor 37 (Bruck, Germany) equipped with an MCT detector. The experimental details for these characterizations can be found in Supplementary Material. Besides, the catalytic performance evaluation processes and operando DRIFTS investigations were given in Supplementary Material.

2.3. Density functional theory studies

All the density functional theory (DFT) calculations were performed with the Vienna ab initio simulation package (VASP) code [33]. The exchange and correlation energy functional was expressed in the GGA-PBE [34]. The projector-augmented wave (PAW) method was used to describe the interactions between ions and electrons [35]. The valence electrons were solved in the plane-wave basis with a cutoff energy of 400 eV. To accurately describe the localization of Ce 4f electrons, we

Table 1
Positron lifetimes and relative intensities of prepared Pt_1-CeO_2 catalysts.

Sample	τ_1 (ps)	τ_2 (ps)	I_1 (%)	I_2 (%)	I_2/I_1	τ_{av} (ps)[a]
CeO_2{111}	207 ± 6	412 ± 19	79.6 ± 2.7	20.4 ± 2.7	0.26	248.82
CeO_2{110}	240 ± 11	427 ± 10	67.2 ± 3.1	32.8 ± 3.1	0.49	301.34
CeO_2{100}	275 ± 7	406 ± 21	60.7 ± 5.8	39.3 ± 5.8	0.65	326.48
Pt_1-CeO_2{111}	205 ± 3	450 ± 19	81.1 ± 2.1	18.9 ± 2.1	0.23	251.31
Pt_1-CeO_2{110}	234 ± 6	450 ± 21	69.9 ± 4.0	30.1 ± 4.0	0.43	299.02
Pt_1-CeO_2{100}	268 ± 10	453 ± 25	64.2 ± 7.3	35.8 ± 7.3	0.56	334.23

Note: [a]$\tau_{av} = \tau_1 \times I_1 + \tau_2 \times I_2$.

conducted the DFT + U calculations with a value of U_{eff} = 4.5 eV. The setting of Hubbard-like term (U_{eff}) follows the approach explored by Cococcioni and De Gironcoli [36]. The convergence criteria for the energy calculation and structure optimization were set to 1.0×10^{-4} eV and a force tolerance of 0.05 eV/Å, respectively [37]. The Brillouin-zone integration was performed using a 1 × 1 × 1 Γ-centered k-point mesh with Gaussian smearing set to 0.05 eV.

Three common CeO_2 surface terminations of (111), (110) and (100) were chosen for the calculations. The CeO_2(111) surface consisted of p (3 × 3) nine-atomic-layer supercells with the bottom three layers fixed, the CeO_2(110) surface was modeled by p(2 × 3) five-atomic-layer su-percells with the bottom two layers fixed, and the CeO_2(100) surface was modeled by an O-terminated p(3 × 3) seven-atomic-layer super-cells with the bottom two layers fixed [38]. To maintain the stoichio-metry of the CeO_2(100) surface and avoid the dipole moment normal to the surface, a half oxygen monolayer was transferred from the surface to the bottom of the slab [39]. The vacuum space that perpendicular to these surfaces was set to 15 Å to minimize the interaction between distinct slab surfaces.

The adsorption energies were defined by the equation, E_{ads} = E (adsorbate/surface) − E(adsorbate) − E(surface), where E(adsorbate/ surface) is the total energy of a surface interacting with adsorbate, and E(adsorbate) and E(surface) are the energies of the isolated adsorbate and clean surface, respectively. Therefore, a negative value means exothermic adsorption. The more negative the adsorption energy, the stronger the adsorption. Reaction transition states (TS) were calculated with the climbing image nudged elastic band (CI-NEB) method [40]. Frequency analysis was carried out to ensure that there was only a single imaginary frequency for the transition state. The energy barrier (E_{TS}) was defined as the total energy difference between the transition state and the initial structure. The charge density differences were evaluated using the formula $\Delta\rho = \rho_{A+B} - \rho_A - \rho_B$, where ρ_X is the electron density of X.

3. Results and discussion

3.1. Distortion of Pt-O-Ce interface facilitated by strong metal-support interactions

A series of CeO_2 materials were synthesized, each of which consisted predominantly of a specific exposed facet; confirmed by HR-TEM (Fig. S1). Accordingly, CeO_2{100} (nanocube), CeO_2{111} (nanopolyhedra) and CeO_2{110} (nanorod) display clear lattice fringes, with inter-planar spacing equal to 0.27, 0.31 and 0.19 nm, respectively. The FFT (fast Fourier transformation) of exposed facet compares well with the stan-dard CeO_2 crystal planes [26,27,32]. From XRD patterns (Fig. S2), all samples exhibit a fluorite cubic structure with an Fm-3m space group. The peaks centered at 28.5°, 33.8°, 47.4°, 56.3°, 59.1°, and 69.4° are attributed to the (111), (200), (220), (311), (222), and (400) diffrac-tions, respectively [32,41,42]. Following, according to the comparison of the relative intensity of characteristic peaks, the dominating exposed facets over each sample can be concluded. The peaks assigned to (111) and (222) are intense in the CeO_2{111} samples. The peaks of (200) and (400) are intense in the CeO_2{100} samples. The peak linked to (220) is intense in the CeO_2{110} samples. The analysis of XRD patterns and HR-TEM images clearly demonstrates the main exposed facets of CeO_2 supports.

The abundant oxygen vacancies over CeO_2 were constructed through a reduction process, and then the precursor of Pt species was captured by oxygen vacancies under alkali condition. The optimized structures of these CeO_2 materials were subsequently revealed by the-oretical calculation (Fig. S3) and the formation energies of oxygen va-cancy in CeO_2(111), (110) and (100) surfaces were confirmed to be 2.22, 1.43 and 1.69 eV, respectively (Fig. S4). However, the formation energies of oxygen vacancies in CeO_2(111), (110) and (100) sub-sur-faces were determined to be 2.30, 2.72, and 3.36 eV, much higher than that of surface oxygen vacancies (Fig. S4). It is these low oxygen va-cancy formation energies and adsorption energies that allow the Pt atoms are inclined to be stabilized by surface oxygen vacancies. The function of different oxygen vacancies has a significant effect on the performance of single atom materials. Herein, in-depth discussions about the nature of oxygen vacancies and its regeneration processes have been conducted. Cerium oxide can accommodate a high oxygen deficiency by the substitution of lower valent elements on the cation sub-lattice [42,43]. The various kinds of oxygen vacancies not only provided sufficient sites to support active metals, but contributed to oxygen species transport on the surface of materials when involving in the catalytic reactions.

Subsequently, positron annihilation spectroscopy (PAS) was adopted to illustrate that which vacancy plays a key role in trapping Pt atoms. Table 1 provides a list of positron lifespan components (τ_1, τ_2) and corresponding relative strength (I_1, I_2) for the CeO_2 supports and Pt_1-CeO_2 SACs. The shortest-lived component (τ_1) is related to small neutral Ce^{3+}-oxygen vacancy associates and mono-vacancies. The in-termediate component τ_2 comes from oxygen vacancy clusters with large size (i.e., dimmers, trimmers, or larger), as a consequence of the interaction among the small neutral Ce^{3+}-oxygen vacancy associates [32,41,43]. In comparison, the τ_1 positron lifespan components slightly decrease upon the loading process from CeO_2 supports to Pt_1-CeO_2 single atom materials, indicating that the neutral oxygen vacancies especially mono-vacancies are consumed during Pt stabilization. Be-sides, as illustrated, the reduction of I_2/I_1 ratio reveals the exposure of large size defects is enhanced, which accelerates the diffusive process of oxygen anions, and a consecutive supply of oxygen from the bulk to the surface would ensure a promoted reducibility [32]. Based on previous studies, re-adsorption of oxygen on the point defects was much slower than that on the multiple defects, indicating that multiple defects are liable to be occupied with oxygen clusters in rich oxygen conditions

[32]. Therefore, the mono-vacancies are preferred to combine with oxhydryl under alkali conditions, which are decisive to capture the precursor of Pt species ($H_2PtCl_6 \cdot 6H_2O$).

According to the sequential analyses of these substances by HR-TEM (Figs. S5–S7), the Pt nanoparticles cannot be founded in these HR-TEM and HAADF images. It is hard to distinguish the Pt atoms under the TEM experimental conditions. Therefore, the aberration-corrected scanning transmission electron microscopy (ac-STEM) was subse-quently utilized to probe the Pt_1-CeO_2 catalysts (Fig. 1a–c), and in-dividual Pt atoms could be observable as uniformly dispersed. The

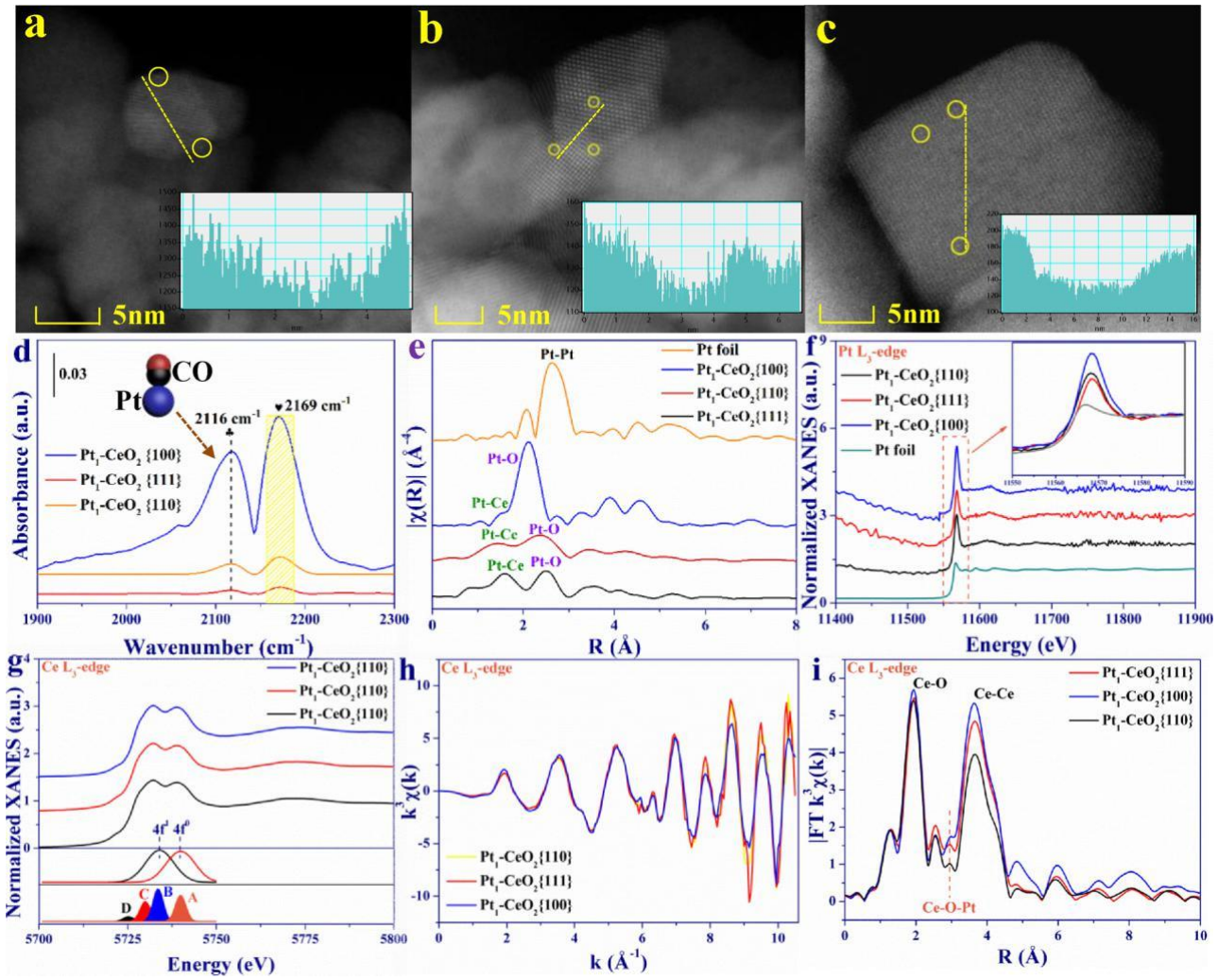

Fig. 1. (a-c) Aberration corrected HAADF-STEM images of Pt_1-CeO_2 materials (the pixel intensity profile was supplied in the insert images); (d) In situ FTIR spectra of CO adsorption over prepared materials; (e) R-space spectra from Pt L_3-edge EXAFS data; (f) Pt L_3-edge XANES spectra; (g) Ce L_3-edge XANES spectra; (h) Corresponding EXAFS fitting curves at the k space; (i) k^3-weighted Fourier transform EXAFS spectra at the R space.

Table 2
Structural parameters of Pt_1-CeO_2 materials extracted from the EXAFS fitting results.

Sample	Pt-Ce			Pt-O		σ^2 (Å^2)	E_0 (eV)[b]
	R (Å)		CN[a]	R (Å)	CN[a]		
Pt_1-CeO_2{110}	1.896	± 0.011	2.13 ± 0.05	2.01 ± 0.002	3.05 ± 0.14	0.003 ± 0.002(Pt)	1.13 ± 0.02
Pt_1-CeO_2{100}	1.901	± 0.005	1.78 ± 0.06	1.98 ± 0.003	2.45 ± 0.05	0.002 ± 0.001(Pt)	1.45 ± 0.06
Pt_1-CeO_2{111}	1.903	± 0.006	2.01 ± 0.11	2.03 ± 0.008	2.32 ± 0.18	0.007 ± 0.001(Pt)	1.56 ± 0.03

Note: [a] Integer number constrained. [b] Constrained to be equal for same fit. R is interatomic distance (the bond length between central atoms and surrounding coordination atoms); CN is the coordination number; σ^2 is Debye-Waller factor (a measure of thermal and static disorder in absorber-scatterer distances); E_0 is edge-energy shift (the difference between the zero kinetic energy value of the sample and that of the theoretical model).

abundant representative ac-STEM images were supplied to clearly identified the existence of single atoms over prepared Pt_1-CeO_2 samples (Fig. S8). Subsequently, further characterization of these materials was conducted by infrared spectroscopy, utilizing CO as the probe molecule. In Fig. 1d, the adsorption bands centered at 2169 cm^{-1} at room tem-perature are attributed to the gaseous carbon monoxide adsorbed over the surface of catalysts. The obtained adsorption peaks at 2116 cm^{-1} are the evidence of CO in the presence of atomically dispersed Pt [21,44,45]. Importantly, XAFS as an authoritative method is very re-levant to get further proof of the single atom statues, as displayed in Fig. 1e and Table 2. The prominent peak centered at around 1.89–1.90 and 1.98–2.03 Å are assigned to the Pt-Ce and Pt-O contribution, re-spectively. Almost no Pt-Pt contribution is observed [46–48]. The co-ordinations of Pt atoms with Pt-Ce and Pt-O bonding are included in Table 2. To be specific, the Pt_1-CeO_2{100} sample exhibits a Pt-O co-ordination number of 2.45 ± 0.05 with a radial distance of 1.98 ± 0.003 Å and possesses a Pt-Ce coordination number of 1.78 ± 0.06 with a radial distance of 1.901 ± 0.005 Å.

An in-depth analysis of the electronic metal-support interaction is the fundamental of understanding the stabilization mechanism in this active interface. Herein, a great number of methods were then devel-oped that involved electronic structure analysis of Pt_1-CeO_2 SACs. The Pt L_3-edge normalized XANES (Fig. 1f) revealed the electronic states

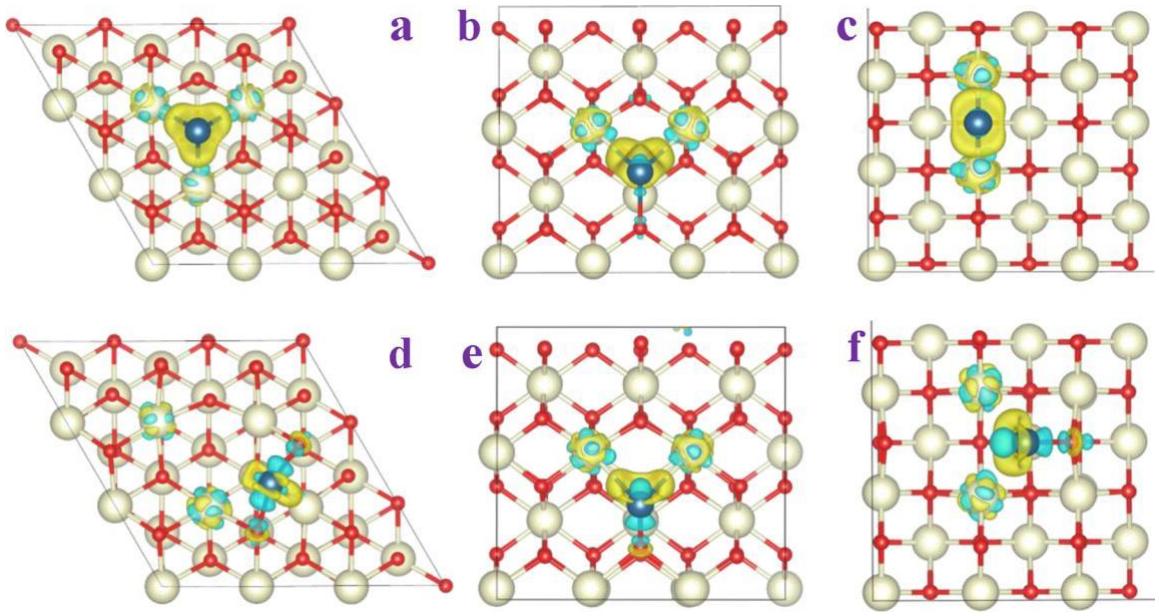

Fig. 2. Calculated charge density differences of (a) Pt_1-undistorted-CeO_2{111}, (b) Pt_1-undistorted-CeO_2{110}, (c) Pt_1-undistorted-CeO_2{100}, (d) Pt_1-distorted-CeO_2{111}, (e) Pt_1-undistorted-CeO_2{110}, and (f) Pt_1-undistorted-CeO_2{100}.

above the Fermi level concentrated on platinum. Since the density of unoccupied 5d electronic states can be probed by the L3 transition, it is widely accepted to use the white-line (WL) intensity as an indicative index for the oxidation state of Pt [49]. Obviously, the Pt_1-CeO_2 sam-ples have significantly higher WL intensities than Pt foil, implying more Pt d-band vacancies and consequently a larger amount of Pt with po-sitive charge centering in prepared SACs, which is attributed to the electron transfer through strong metal-support interaction after Pt atoms stabilized [49,50]. The positively charged intensity of Pt over prepared SACs increased in the order of Pt_1-CeO_2{111} < Pt_1-CeO_2{110} < Pt_1-CeO_2{100}, illustrating that the mutual action be-tween Pt atoms and CeO_2 supports is impacted by the exposed facet of CeO_2 due to its diverse electronic structures. In addition, the systematic edge change of the Pt L_3 edge over Pt_1-CeO_2{100} towards higher en-ergy, implying that the electron donation extent of Pt to CeO_2 support is the most intense among all SACs [50].

From Ce L_3-edge normalized XANES spectra (Fig. 1g), all of the major bands presented a double white line characteristic of a mixture of the two cerium ground-state electronic configurations, $4f^0$ and $4f^1$ [51]. In order to eliminate the influence from the background, all spectra involve subtraction of an arctangent function, and then Gaussian functions are used fitness. These exhibit two evident peaks often marked as A and B. Peak A is assigned as a Ce^{4+} peak with the final state $2p^54f^05d^1$, indicating an excitement for an electron from the Ce 2p
shell to its 5d shell, with an absence of an electron in the 4f shell [51,52]. Peak B is a Ce^{4+} peak as well, but with a different final state of $2p^54f^15d^1$v, indicating another excited electron from the valence band (O 2p shell) to the Ce 4f shell besides a similar one with peak A, and a hole (v) is generated in the valence band. Peak C is occasionally termed as a Ce^{3+} peak [51,52]. An extra minor peak (D) exists at pre-edge and possibly is caused by transitions to the bottom of the conduction band [51,52]. Direct details on the fraction of Ce present as Ce^{3+} can be found from the ratio region of peak C (related with Ce^{3+}) and the total region of peak A, B, and C (A and B are related with Ce^{4+}). The en-hancement of Ce^{3+} ratio for SACs is ascribed to the balancing of Fermi level and charge density between Pt atoms and CeO_2 support through strong metal-support interaction, which was determined by fitting of the Lorentzian peak (Figs. 1h and S9). A peak around 1.8 $Å^{-1}$ corre-sponds to single scattering from first shell oxygen atoms. The peaks detected at 1.8 and 9.4 $Å^{-1}$ are attributed to the refinement of first and higher neighbor correlation [51,52]. The difference intensity of de-tected peaks probably attributes to the crystal size of CeO_2 particle. In addition, as displayed in Fourier transform magnitudes of Ce L_3-edge EXAFS (Fig. 1i), the Ce-O and Ce-Ce path are linked with the signal at 1.9 and 3.6 Å, respectively [53]. Importantly, the band detected at 2.9 Å is assigned to the Ce-O-Pt [52]. It is reasonably supposed that the structure is taken into distortion under strong metal-support interaction from curve-fitting analysis of our XAFS results.

The formation of Pt-O-Ce interface after Pt atoms stabilized in de-fects and the balance of charge density through SMSIs was detailed by the theoretical thermodynamic analysis. The modeling structures of Pt atoms adsorbed at oxygen vacancies over CeO_2 surfaces are shown in Fig. S10. On these surfaces, Pt atoms are connected by surrounding Ce and the adsorption energies of Pt are found to be −4.00, −3.29, and −3.48 eV over the Pt_1-undistortion-CeO_2(111), (110) and (100) sur-faces, respectively. Notably, we observed that the Pt-O-Ce interfaces are inclined to distort for thermodynamic stable through the metal-support strong interaction (Fig. S11), where single atom Pt is connected with Ce and surface O atoms. The intense electron transfers in these distorted Pt-O-Ce interfaces are quantified. On the interface of Pt_1-distorted-CeO_2(111), the shift of Pt takes endothermic energy of 0.72 eV. However, the Pt_1-distorted-CeO_2(110) and Pt_1-distorted-CeO_2(100) surfaces are identified to form more easily with the exothermic energy of −0.64 and −0.74 eV. The results illustrate that the structure dis-tortion process over Pt_1-CeO_2{100} sample tends to occur sponta-neously. To further investigate the changes of electronic structure and valence state during interface distortion, the charge density difference (CDD) was calculated and given in Fig. 2. Combined with the magnetic moment of Ce, single atom Pt gets the charge and shows the valence of -2 with no Ce^{4+} have been reduced on the surface of Pt-undistorted-CeO_2 catalysts. When the interface shifted, the balance of charge den-sity increase and reduction, and the change of magnetic moment of Ce indicate that Pt shows the valence of 0 with two Ce^{4+} have been re-duced to Ce^{3+}.

Ce species in these SACs were presented in mixed Ce^{3+} and Ce^{4+} valence states and the existence of Ce^{3+} was primarily ascribed to the balance of charge density during interface distortion. Therefore, the content of Ce^{3+} species can be seen as an indicator of the distorted degree over prepared SACs [54,55]. The distortion degree in this study is defined for evaluating the intensity and extent of the surficial

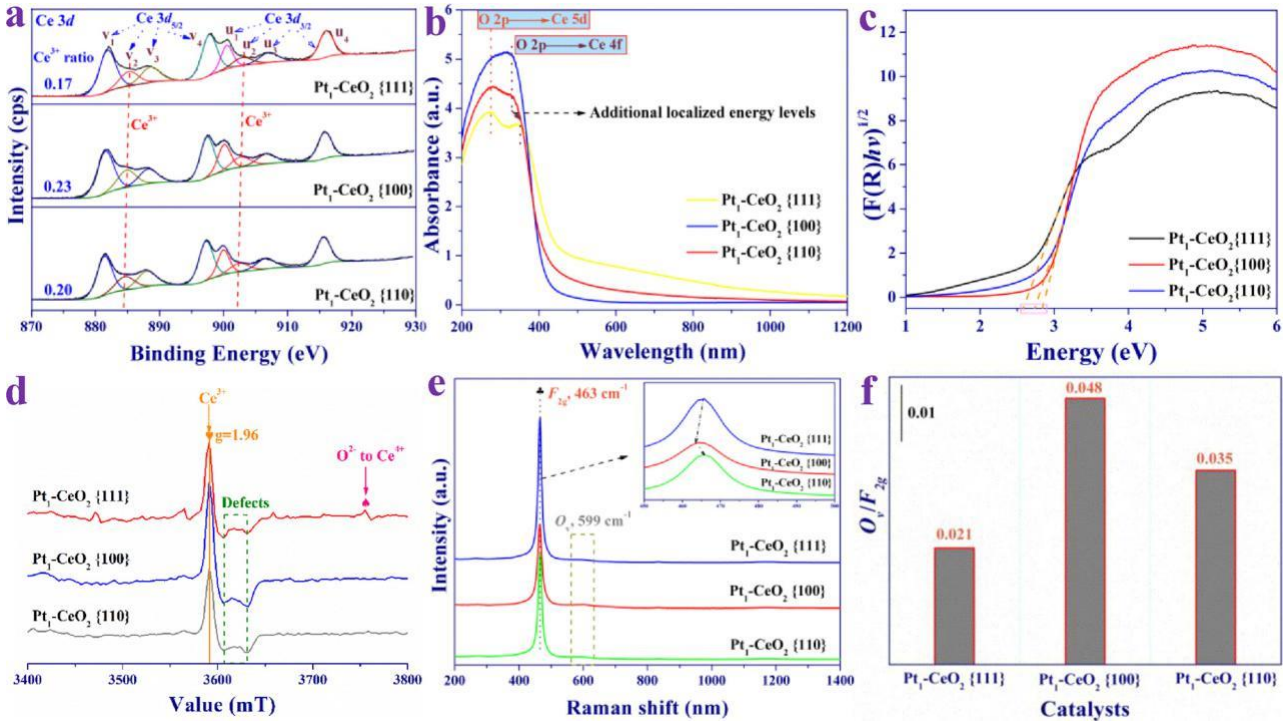

Fig. 3. (a) Ce 3d XPS spectra of Pt_1-CeO_2 materials; (b) UV–vis absorption spectrum of Pt_1-CeO_2 catalysts; (c) The optical bandgap of prepared samples evaluated by liner extrapolating; (d) Electron paramagnetic resonance of Pt_1-CeO_2 samples; (e-f) Laser Raman spectra of Pt_1-CeO_2 materials.

PteOeCe bonding torsional strength [24,38]. The PteOeCe bonding will transform the original bonding structure and angle as the function of the stabilization process. The higher distortion degree in the single atom Pt_1-CeO_2 catalysts means that the PteOeCe bonding exhibits the more intense deformation through a strong metal-support interaction process compared with its origin combination methods. XPS data have been reported as another evidence for proving the resulting variation of valence states through SMSIs in these SACs (Figs. 3a, S12–S13). For Ce 3d spectra (Fig. 3a), the deconvoluted peaks of v_1, v_2, v_3, v_4 were a consequence of the Ce $3d_{5/2}$ region, and the labeled peaks of u_1, u_2, u_3, u_4 resulted from the Ce $3d_{3/2}$ region [56]. In detail, the peaks signed as v_2 and u_2 corresponded to the Ce^{3+} valence species and the other signed peaks were Ce^{4+} valence species [56,57]. The proportion of $Ce^{3+}/(Ce^{3+}+Ce^{4+})$ in each catalyst was then evaluated quantitatively and the ratios were obtained as 0.23, 0.20, and 0.17 for the Pt_1-CeO_2{100}, Pt_1-CeO_2{110}, and Pt_1-CeO_2{111} catalysts, respectively, which can be listed as an indicator for the sequence of interface dis-tortion intensity. Notably, Pt_1-CeO_2{100} exhibited the highest ratio of Ce^{3+}, attributing to the most intensity of electron transfer in the dis-torted interface during SMSIs among these samples, which is generated by balancing Fermi energy level between the Pt species and CeO_2 supports.

The electron transfer process in the distorted interface was further verified by the UV–vis absorption spectra, given in Figs. 3b and S14. Two strong absorption bands centered at about 296 and 335 cm^{-1} were ascribed to the charge-transfer transition from O 2p to Ce 5d orbital and O 2p to Ce 4f orbital, respectively [58,59]. The optical bandgaps cal-culated based on the UV–vis absorption spectra of Pt_1-CeO_2{100}, Pt_1-CeO_2{110}, and Pt_1-CeO_2{111} are 2.85, 2.75, and 2.58 eV, respec-tively (Fig. 3c). The redshift of Pt_1-CeO_2{100} is attributable to the extra concentrated energy levels (oxygen vacancies) within the bandgap, absorbing with relatively low energy photons, which was further proved by electron paramagnetic resonance (Fig. 3d). The extra strong resonance line at g = 1.96 is assigned to the responding of Ce^{3+} species [60,61]. This increased intensity of Ce^{3+} single over Pt_1-CeO_2{100} sample is attributed to the decrease of Ce^{4+} ions to Ce^{3+} with electrons produced by the structure distortion; moreover, this protruding electron is also inclined to trapped in oxygen vacancies around distortion interface, which gives a characteristic peak at about 3610–3630 mT in EPR spectra [60,61]. The abundant oxygen vacancies promoted by the distorted Pt-O-Ce interface were valued by Raman spectra accordingly. As displayed in Fig. 3e, the abrupt strong peak approximately 463 cm^{-1} and another weak one at 603 cm^{-1} result from the oxygen atoms symmetric strengthen (the fluorite structure, F_{2g} signal) and Frenkel-typeanion defects (O_v), respectively [56,57,59,60]. The blue shift of F_{2g} peak from Pt_1-CeO_2{100} to Pt_1-CeO_2{110} and Pt_1-CeO_2{111} indicates the enhancement of defects content [41,59,60]. In-depth, the concentration of the oxygen vacancy is in-dexed with the relative ratio between the defect band and the F_{2g} signal [57]. As shown in Fig. 3f, the highest O_v/F_{2g} value is confirmed over the Pt_1-CeO_2{100} sample, revealing that the enhanced distortion of in-terface greatly promoted the generation of defects around it.

The above experimental and theoretical results illustrate that upon Pt atoms are stabilized in surface mono-defects, and the formed Pt-O-Ce interface will be taken into distortion spontaneously to keep thermo-dynamics stable through strong metal-support interactions. This inter-action is combined with the balance of charge density, which brings about the variation of valence state and electronic structure of SACs. The ratio of Ce^{3+} species is a clear positive correlation with the dis-tortion degree of the interface, which is predictable given the fact that this species is known as a crucial factor for stabilizing of single atom sites in thermal reactions.

3.2. Oxygenated hydrocarbon oxidation over Pt_1-CeO_2 single atom catalysts

The catalytic performance of Pt_1-CeO_2 materials with distorted Pt-O-Ce interfaces was determined for oxygenated hydrocarbons removal (Fig. 4 and Table S1). We claimed that the Pt_1-CeO_2{100} material exhibits excellent decomposition efficiency (Fig. 4a), over which 90 % of methanol (700 ppm) could be decomposed (T_{90}) at just 52 °C, much lower than that of Pt_1-CeO_2{110} (T_{90} of 68 °C) and Pt_1-CeO_2{111} (T_{90}

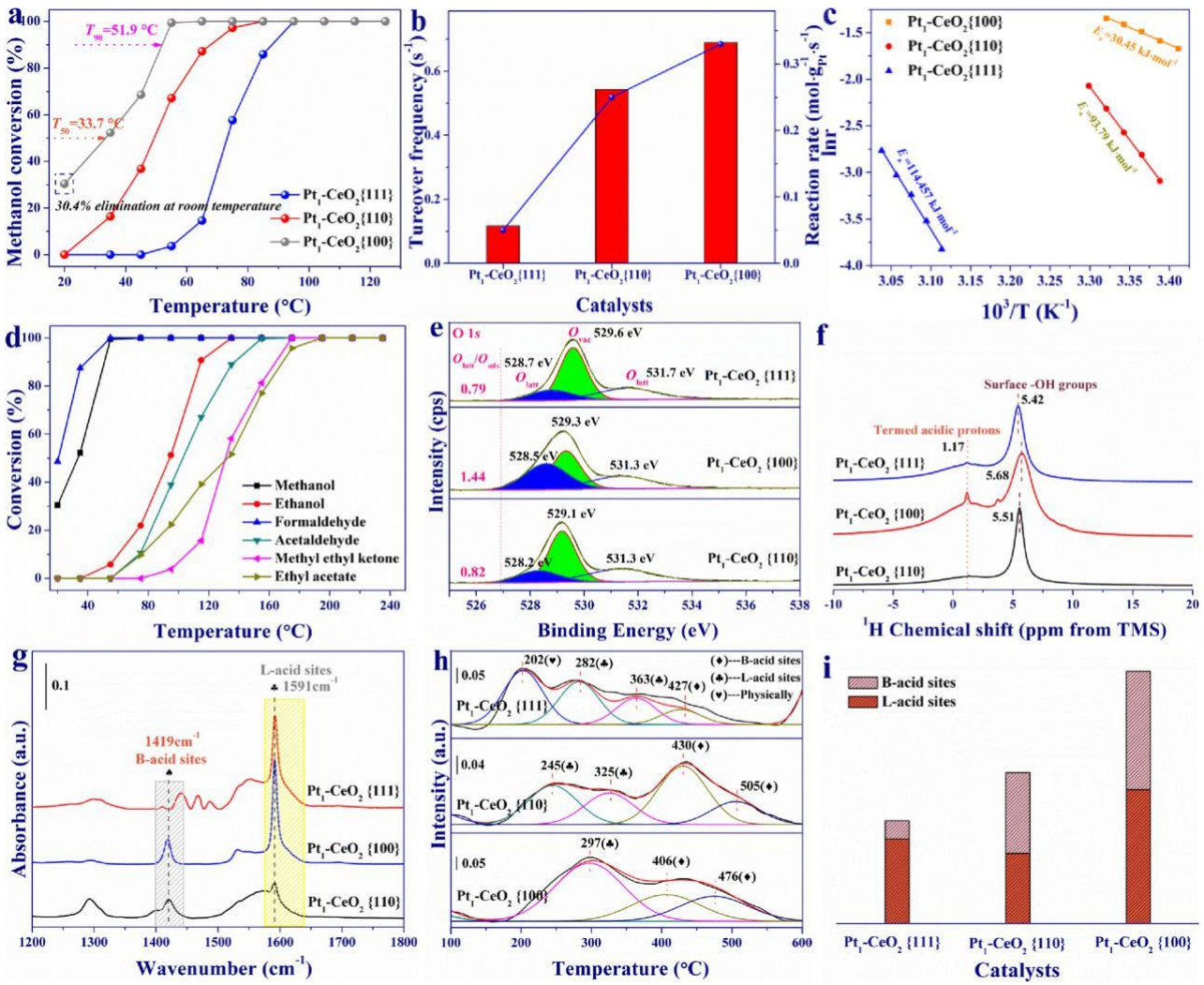

Fig. 4. (a) Catalytic performance of methanol oxidation over prepared Pt_1-CeO_2 materials; (b) Reaction rate and turnover frequency for methanol oxidation over active catalysts at 50 °C; (c) Arrhenius plots of methanol oxidation over Pt_1-CeO_2 catalysts; (d) Light-off curves of typical oxygenated hydrocarbons decomposition over Pt_1-CeO_2{100} material; (e) O 1s XPS spectra of Pt_1-CeO_2 catalysts; (f) ^{1}H solid-state MAS NMR spectra of Pt_1-CeO_2 materials; (g) NH_3-IR experiments over Pt_1-CeO_2 materials; (h,i) Temperatured programmed desorption of NH_3 for Pt_1-CeO_2 material.

of 88 °C) samples, which is a significantly lower temperature than ty-pical active materials reported for methanol oxidation, e.g., 3.5 wt.% Au/Fe_2O_3 (T_{90} of 150 °C), 1.5 wt.% Pd/HY (T_{90} of 130 °C) and Pt_1-Co_3O_4 (T_{90} of 96 °C) catalysts (Table S2). A subsequent estimation for the reaction rate and turnover frequency (TOF) of Pt supported cata-lysts was provided. A reaction rate of 0.33 mol·gPt^{-1}·s^{-1} at 55 °C was determined for Pt_1-CeO_2{100} material, which is higher than that ob-served over Pt_1-CeO_2{110} (0.25 mol·gPt^{-1}·s^{-1}) sample and over 6 times higher than Pt_1-CeO_2{111} (0.05 mol·gPt^{-1}·s^{-1}) catalyst (Figs. 4b and S15). The TOFs exhibited were based on the dispersion of Pt in each catalyst (Figs. 4b and S16). The results clearly reveal that the activity of all Pt sites in Pt_1-CeO_2{100} catalyst (0.68 s^{-1} at 50 °C) was sub-stantially improved, which has a larger value over the other catalysts in previous literature on this reaction until now; particularly, 3.3 and 2.5 times higher than that reported over Pd/CeO_2-ZrO_2 (0.22 s^{-1}) and Pt_1-Co_3O_4 (0.29 s^{-1}) catalysts (Table S2). Based on this data, Arrhenius plots were extracted and apparent activation energy (E_a) was de-termined for methanol oxidation (Fig. 4c). The E_a of Pt_1-CeO_2{100} catalyst (30.45 kJ mol^{-1}) is substantially lower than that of Pt_1-CeO_2{110} (93.79 kJ mol^{-1}) and Pt_1-CeO_2{111} (114.46 kJ mol^{-1}) catalysts. The Pt_1-CeO_2{100} SAC with the highest distortion intensity exhibits the best catalytic efficiency for methanol oxidation; as ex-pected, which was adopted to decompose typical oxygenated hydrocarbons as proof of its universality, as displayed in Fig. 4d. For each of the substrates investigated, current literature reported catalysts are also displayed for comparison, as summarized Tables S3–S6. As demonstrated, the prepared Pt_1-CeO_2{100} catalyst exhibits consider-able efficiency for the oxidation of formaldehyde, acetaldehyde, ethanol, methyl ethyl ketone, and ethyl acetate at low temperature (< 200 °C), compared with previously reported works.

According to the observed activity of Pt_1-CeO_2 SACs, analysis is performed for detailed correlation between catalytic performance and structural properties including: high quantity of lattice oxygen (Fig. 4e), abundant surface acid sites (Fig. 4f–i), sufficient surface-bound hy-droxyl species (Fig. 4f), low temperature reducibility (Fig. S17), sui-table oxygen/methanol adsorption capacity (Figs. S18 and S19) and an abundance of oxygen vacancies (Fig. 3e, f and Table 1). According to the theoretical studies and experiment data involved in this work, we point out that the evident rise in the amount of lattice oxygen species and surface acid sites over the Pt_1-CeO_2{100} catalyst is possibly the utmost factor for improving the catalytic performance [6–8,12]. As shown in Fig. 4e, a fitting for O 1s XPS spectra of all materials reveals three peaks with binding energies of approximately 528.7, 529.6, and 531.7 eV, which can be associated with the lattice oxygen (O_{latt}), oxygen vacancy (O_{vac}), and surface adsorbed oxygen (O_{ads}), respec-tively [62,63]. The relative content of surface oxygen vacancies over all

three samples was enhanced with the order of Pt_1-CeO_2{100} < Pt_1-CeO_2{110} < Pt_1-CeO_2{111}, which is ascribing to the more surface small neutral oxygen vacancies are occupied by the single atoms Pt sites in Pt_1-CeO_2{100} sample. It is widely known that with certain catalysts, lattice oxygen plays an important role in catalytic performance in the oxidation of hydrocarbons [4–6]. The results are quite noteworthy from quantification of the peaks attributed to lattice oxygen and surface adsorbed oxygen. The O_{latt}/O_{ads} ratio of Pt_1-CeO_2{100} material is calculated to be 1.44, which is noticeably higher than that of Pt_1-CeO_2{111} (O_{latt}/O_{ads} = 0.79) and Pt_1-CeO_2{110} (O_{latt}/O_{ads} = 0.82) catalysts.

For evaluating the acid sites of prepared SACs, ^{1}H solid-state MAS NMR (Fig. 4f) was subsequently incorporated to identify the unit structure of prepared materials. For these materials, the foremost peak observed at a chemical shift of roughly 1.17 ppm is attributable to the termed acidic protons and bands at around 5.42–5.68 ppm could in-dicate the asymmetric stretching of surface hydroxyl [64,65]. The en-hanced intensity of characteristic peaks illustrates that the Pt_1-CeO_2{100} material possesses substantial proton-provided acid sites. The corresponding kind of acid species of all the materials was further estimated by NH_3-IR (Fig. 4g) and NH_3-TPD (Fig. 4h, i). For NH_3-IR experiments (Fig. 4g), the bands detected at 1419 and 1591 cm^{-1} could be used as an indication for the symmetric vibrations of NH^{4+} species on Brønsted acid sites and Lewis acid sites, respectively. The most in-tense peaks of NH_3 adsorption over Pt_1-CeO_2{100} sample illustrates that the enhanced amount and intensity of acid sites over the materials [6]. Furthermore, a subsequent deconvoluted with the Gauss curve fitting method for the NH_3-TPD profiles of materials provides several peaks (Fig. 4h) corresponding to the physically-adsorbed NH_3 (< 220 °C), ammonia-adsorbed on Lewis acid sites (240–380 °C) and ammonia-adsorbed on Brønsted acid sites (> 400 °C) [6]. Accordingly, the quantitative assessment of different acid species was evaluated by counting the peak area of NH_3-TPD experiment, as shown in Fig. 4i. The prepared Pt_1-CeO_2{100} SAC exhibits the maximum amount of Brønsted acid sites and Lewis acid sites [6]. The promoted Lewis acid sites correlate to the formation of oxygen vacancies; meanwhile, the abundant Brønsted acid sites promote VOC molecules adsorption and accelerate the regeneration of surface hydroxyl, which is benefit for intermediates decomposition during VOC oxidation.

3.3. Stabilizing Pt atoms by Pt-O-Ce interface distortion

The stability (especially; thermal and reaction stability) of a single atom catalyst is crucial for its application in thermal reactions. In this work, the electronic metal-support interaction in Pt-O-Ce interface is responsible for stabilizing Pt atom in Pt_1-CeO_2 materials (Fig. 5a). In order to explore the reaction stability of SAC materials, an extra study was performed where the catalytic performance was monitored for an extended 800 min at 52 °C in a mixture airflow, as displayed in Fig. 5b. Negligible deactivation can be observed for all catalysts, suggesting their excellent reaction stability in the total oxidation of methanol. As CO_2 is one of the reaction products, commonly present in industrial exhaust streams, it is of significance to clarify its influence on the long-term oxidation behavior of the SACs. As illustrated in Fig. 5c, CO_2 ex-hibited a detrimental effect on methanol oxidation ascribed to the strong adsorption of CO_2, methanol, and O_2 molecules on the catalyst surface. When 3vol.% CO_2 was introduced into the stream, the reduc-tion of methanol conversion of ca. 4.6 %, 10.7 %, and 5.8 % can be observed over Pt_1-CeO_2{100}, Pt_1-CeO_2{110} and Pt_1-CeO_2{111} samples, respectively. Importantly, the original activity was restored after only 40−50 min of cutting off CO_2 in the feed, indicating that the decreases in activity are used as evidence for permanent changes to the SACs.

In order to determine whether these catalysts undergo thermal de-activation, the prepared SACs were annealed at different temperatures (300, 400, 600, and 800 °C) in air and the catalytic performance of resulting materials are shown in Fig. 6a–c. Obviously, the Pt_1-CeO_2{100} material possesses the highest thermal stability among these SACs, which displays the similar catalytic efficiency after calcinated at 300 or 400 °C and maintains 70 % catalytic efficiency (at 125 °C) after annealed at 800 °C. However, the activity of both Pt_1-CeO_2{110} and Pt_1-CeO_2{111} catalysts decreased greatly after annealed at 600 or 800 °C. For instance, the methanol oxidation efficiency (at 125 °C) de-creased to 29 % and 17 % after annealed at 800 °C for Pt_1-CeO_2{110} and Pt_1-CeO_2{111} samples, respectively. In order to illustrate the changes of single atom sites and CeO_2 supports after the annealed process at 800 °C, the HR-TEM and HAADF images were supplied (Figs. S20 and S21). The microstructure and lattice parameters remain un-changed during the thermal treatment at 800 °C in air condition. Nevertheless, the apparent agglomeration of Pt species was revealed by ac-STEM after this re-calcination process. Additionally, the variation of Pt sites over the re-calcined SACs was examined by the CO-IR experi-ment (Fig. 6d, f). The Pt atoms over Pt_1-CeO_2{110} and Pt_1-CeO_2{111} catalysts are totally converted into nanoparticles after annealed at 600 °C; in comparison, the characteristic peak of CO adsorption over Pt atoms can still be detected for Pt_1-CeO_2{100} sample calcined at 800 °C. The agglomeration of Pt single atoms is the dominant reason for catalyst deactivation under thermal conditions. The Pt atoms stabilized in CeO_2{100} facet can prevent its agglomeration to some extent.

As discussed above, the prepared SACs exhibit the stability order of Pt_1-CeO_2{100} > Pt_1-CeO_2{110} > Pt_1-CeO_2{111}, consistent with the distortion degree of each active interface. Accordingly, in this work, the designed Pt atoms were stabilized in the exposed oxygen vacancies over CeO_2 support, and then the formed Pt-O-Ce interface will be taken into distortion to keep the thermodynamic stable state, which is the result of strong metal-support interactions and combining with the balance of charge density. Based on the electronic structure analysis of prepared SACs (Fig. 3), the most intense of charge transfer was revealed between Pt atoms and CeO_2{100} facets, which confirmed the outstanding sta-bility under thermal and reaction conditions in this Pt-O-Ce interface.

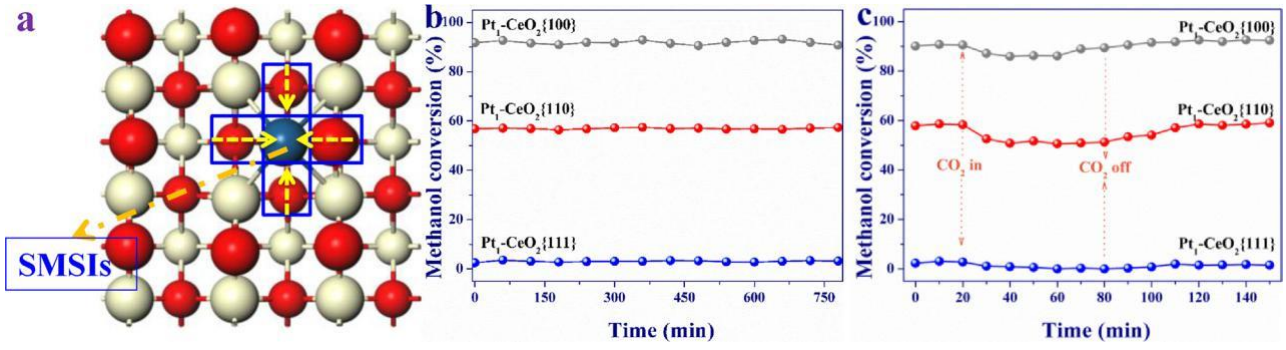

Fig. 5. (a) Optimistic structure of distorted Pt-O-Ce interface over Pt_1-CeO_2{100} catalyst; (b) Reaction stability and (c) CO_2-resistance tests of prepared Pt_1-CeO_2 materials for methanol oxidation at 52 °C.

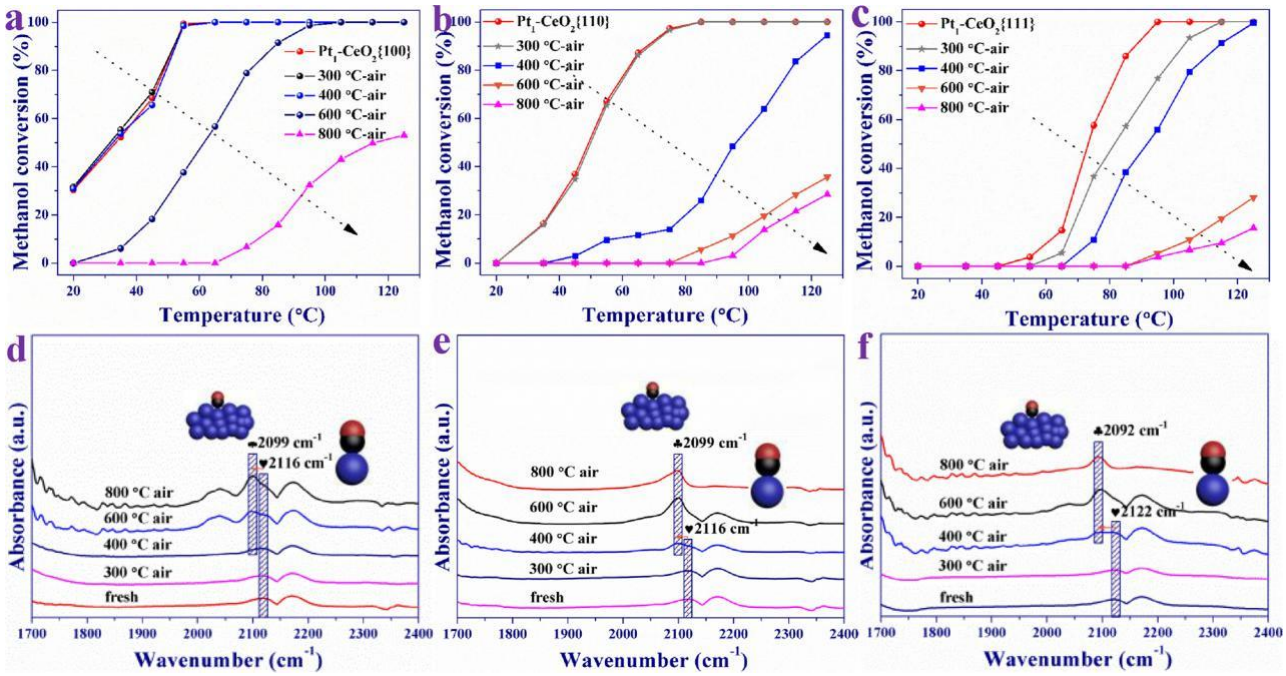

Fig. 6. (a-c) The catalytic performance for methanol oxidation over prepared Pt_1-CeO_2 materials after annealing at different temperatures; (d-f) CO-IR experiments of prepared Pt_1-CeO_2 materials after annealing at different temperatures.

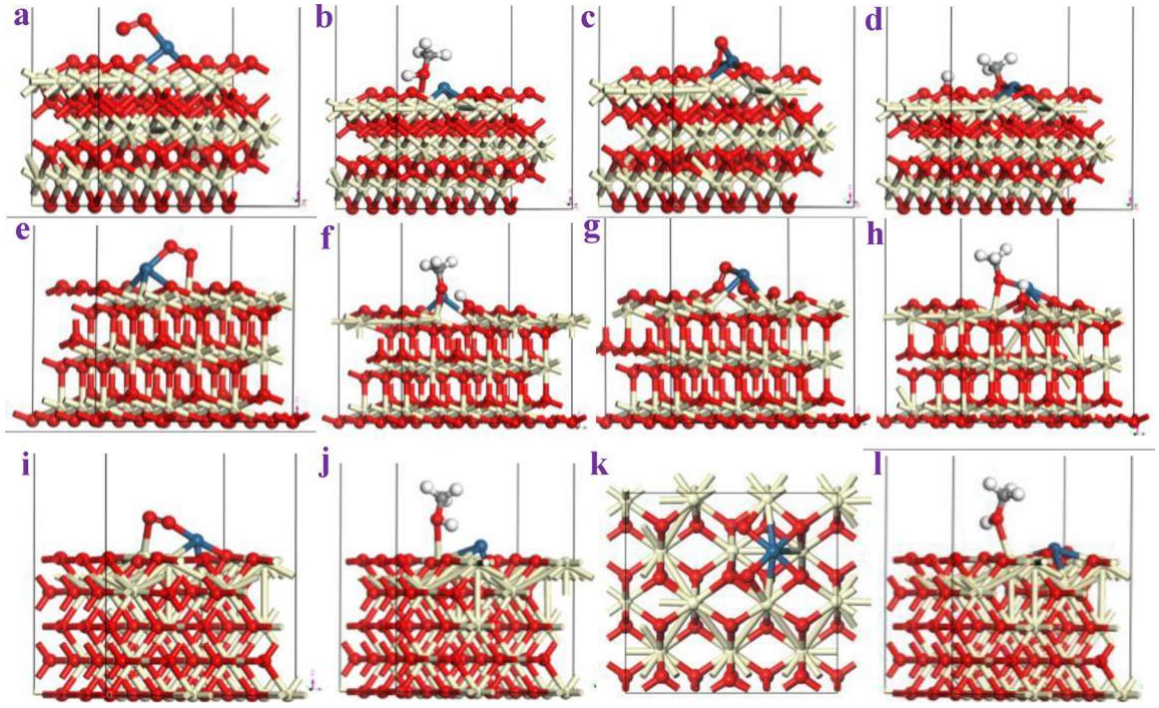

Fig. 7. The optimistic structure of O_2 adsorption over (a) Pt_1-undistorted-CeO_2(100), (c) Pt_1-distorted-CeO_2(100), (e) Pt_1-undistorted-CeO_2(111), (g) Pt_1-distorted-CeO_2(111), (i) Pt_1-undistorted-CeO_2(110), and (k) Pt_1-distorted-CeO_2(110) materials; The optimistic structure of methanol adsorption over (b) Pt_1-undistorted-CeO_2(100), (d) Pt_1-distorted-CeO_2(100), (f) Pt_1-undistorted-CeO_2(111), (h) Pt_1-distorted-CeO_2(111), (j) Pt_1-undistorted-CeO_2(110), and (l) Pt_1-distorted-CeO_2(110) materials (red, gray, white, faint yellow, and indigo spheres represents the O, C, H, Ce, and Pt atoms, respectively) (For interpretation of the references to colour in this figure legend, the reader is referred to the web version of this article).

The distortion of the active interface significantly promotes the capacity of methanol and O_2 adsorption, which is regarded as another crucial reason for improving the stability of SACs. The adsorption en-ergies and configurations of CH_3OH and O_2 on the Pt_1-CeO_2 surfaces were shown in Figs. 7, S22–S23, and Table 3. On the surfaces of Pt_1-undistorted-CeO_2 catalysts, CH_3OH and O_2 molecules adsorb on them with low adsorption energies (> -1.0 eV). Two exceptions of O_2 ad-sorption on Pt_1-undistorted-CeO_2(110) and CH_3OH adsorption on Pt_1-undistorted-CeO_2(100) are due to the occurrence of Pt atom shift and structural distortion after O_2 and CH_3OH adsorption. It can be found in Table 3 that the adsorption energies of CH_3OH and O_2 on Pt_1-distorted-CeO_2 catalysts are higher than Pt_1-undistorted-CeO_2 catalysts.

Table 3
CH_3OH and O_2 adsorption on Pt_1-CeO_2 surfaces.

E_{ads} (eV)	Pt_1-CeO_2(111)		Pt_1-CeO_2(110)		Pt_1-CeO_2(100)	
	undistorted	distorted	undistorted	distorted	undistorted	distorted
CH_3OH-ads	−0.36	−2.33	−0.66	−1.92	−1.66	−3.45
O_2-ads	−0.41	−1.91	−3.01	−2.37	−0.17	−2.61

Particularly, for CH_3OH adsorption on Pt-distorted-CeO_2 catalysts, the O-H of CH_3OH ruptures spontaneously with O and H connected with Ce/Pt and surface oxygen (O_s), respectively. Among them, CH_3OH has the strongest adsorption ability on the surface of Pt_1-distorted-CeO_2(100). For O_2 adsorption on Pt_1-distorted-CeO_2 catalysts, the oxygen molecules fill the exposed oxygen vacancies and connect with neighboring Ce and Pt. The Pt_1-distorted-CeO_2(100) surface also pos-sesses the strongest O_2 adsorption. The electronic metal-support inter-action in this distorted interface is integrant for stabilizing Pt atom in Pt_1-CeO_2 materials, which will promote the development and applica-tion of stable single atom materials in thermal catalytic reactions.

3.4. The intrinsic mechanism for methanol oxidation

The oxidation mechanism and reaction pathways are crucial for the wide application of SACs in hydrocarbon oxidation [6–8,12]. Therefore, the methanol oxidation mechanism over prepared Pt_1-CeO_2 materials is explored by in situ experiments and DFT studies. In this work, the oxidation of methanol follows a first-order reaction due to the excess of oxygen in the reaction system [12]. As displayed in Fig. 8a–c, the peaks at around 3603−3744 cm^{-1} are assigned to the strengthening of sur-face hydroxyl [6]. The bands between 2780 and 2994 cm^{-1} are asso-ciated with the C–H bond vibration; thereinto, the frequency centered at 2830 and 2953 cm^{-1} are attributed to the δ(C–H) and ζ(C–H) from $-CH_2/-CH_3$ groups, respectively [66,67]. The confirmation of meth-oxyl groups ($-CH_3O$) was centered at 1021 or 1033 cm^{-1}, primarily coming from the O–H bond activation over the active interface [67–69]. The stretching of $-CH_2O$ groups was formed due to the breakage of C–H bond over methoxyl, which is in line with our previous study [12]. However, the monitored peaks appearing at a relative low temperature around 1060-1090 cm^{-1} are indicative of a bridging mode of asymmetrical carbonyl (-C = O) groups, which evidently vanishes with temperature increasing [68,69]. This phenomenon strongly in-dicates that the methanol oxidation processes obey different reaction paths along with temperature ranging. In addition, the detected peaks at 1373 cm^{-1} belong to the signal of dioxy-methylene ($-CH_2OO$) groups [65,68,69]. The observed sharp peaks at around 1587 or 1588 cm^{-1} are associated with carboxyl species (−OCO), which may mainly from the dissociation of dioxy-methylene (DOM) intermediates [66,68,69].

For in-depth analysis of reaction mechanism, we carried out the in situ DRIFTS experiments by switching the reaction conditions at tem-peratures of T_{15} and T_{85} during methanol oxidation. As provided in Fig. 8d–f, the methoxyl species are not impacted by changing reaction atmosphere and the peaks of carbonyl groups take the lead at the be-ginning of reaction in N_2 condition. Obviously, the enhanced intensity peaks at 1373 and 1587/1588 cm^{-1} correlate to an increase of DOM and carboxyl species when the air was introduced into the reaction system (the band of carbonyl disappeared in the presence of air). When the N_2 source was re-filled into the reaction cavity, the intermediates are shown to be recovered similarly with the beginning stage. The above results verify that the methanol activation obeys the L-H me-chanism under relative low temperatures [7]. In this condition, the surface adsorbed oxygen is adopted as the active oxygen species, which participate in the activation and the DOM (1373 cm^{-1}) and carboxyl (1587/1588 cm^{-1}) species are produced as the main intermediates.

When the surface oxygen is less, the methanol molecule was decom-posed through step broken of the C–H bond in this condition. Inter-estingly however, differences in the spectra can be seen for the me-thanol oxidation mechanism over the mono-dispersed Pt-O-Ce interface with the temperature increasing (Fig. 8g–i). Changing the reaction at-mosphere at 150 °C did not obviously affect the formation of DOM (1373 cm^{-1}) and carboxyl (1587/1588 cm^{-1}) species during methanol decomposition, suggesting that these species are mainly generated by the lattice oxygen. It can be concluded that the methanol oxidation at high temperature obeys the MVK mechanism [6,12]. Understandably, the assignments of these vibrational features are ascribed to the dis-tortion of the Pt-O-Ce interface. The Pt atoms are stabilized in the va-cancies and the formation of Pt-O-Ce active interface takes into most stability through the distortion process, which is the result of strong metal-support interaction and combining with the intense electron transfer. The compact mutual effect increases the energy barrier for lattice oxygen activation; therefore, the surface adsorbed oxygen is adopted as the active oxygen species and methanol oxidation obeys the L-H mechanism at relative low temperature. With the temperature in-creasing, the lattice oxygen species from larger oxygen vacancy clusters around Pt atoms sites are activated and promoting the methanol oxi-dation process tremendously.

Accordingly, the activation mechanism of methanol oxidation over the active Pt-O-Ce interface is proposed and summarized in Fig. 8j. The distortion of the Pt-O-Ce interface enhanced the adsorption of methanol molecules. Consequently, the O assisted O–H bond of methanol is ac-tivated, forming adsorbed methoxyl species. It is expected that in this distorted Pt-O-Ce interface, the oxygen species will be supplied at the support/nanoparticle perimeter or on defect sites. Adsorbed methoxyl species undergo β-H transfer with a neighboring O atom and surface hydroxyl group on the surface, forming adsorbed DOM species. The presence of adsorbed DOM molecules is decomposed through a broken process to produce carboxyl intermediates over Pt atoms, which are oxidized into H_2O and CO_2 evidently. The study of the intrinsic me-chanism helps to determine the real active sites during oxidation re-actions over SACs and understand the mechanism in a more compre-hensive view.

According to the results of decomposition routes and analysis of electronic structure upon, the reaction pathway for CH_3OH oxidation on Pt_1-distortion-CeO_2(100) catalyst revealed by theoretical calcula-tions is shown in Fig. 9, comprised of structures of essential inter-mediates and transitional state. For a clear illustration, the complete mechanism for reaction consists of several steps: CH_3OH and O_2 ad-sorption (states (a)-(c)); two-step C–H cleavage (states (TS1)-(e)); H_2O desorption (state (f)); C–H cleavage (state (g)); CO_2 and H_2O desorption (state (h)). After CH_3OH adsorption (state (b)), OH group of CH_3OH molecule dissociate spontaneously ($CH_3OH + O_s \rightarrow CH_3O + O_sH$), and O_2 adsorb on the surface with the energy of -0.09 eV and O–O distance of 1.28 Å (state (c)). With the assistant of adsorbed oxygen species, the H of CH_3O transfers to one oxygen atom with the activation barrier and reaction energy of 0.23 and -1.55 eV, respectively. During this process, the C of CH_2O combines with the other oxygen atom to form CH_2O_2OH group (state (TS1)-(d), $CH_3O + O_2 \rightarrow CH_2O_2OH$). Then, a breakdown happens to the C–H bond of CH_2O_2OH, along with the transfer of H to neighboring OH to produce H_2O (state (TS2)-(e), $CH_2O_2OH \rightarrow CHO_2 + H_2O$). The barrier for the second C–H bond cleavage is 0.44 eV, with

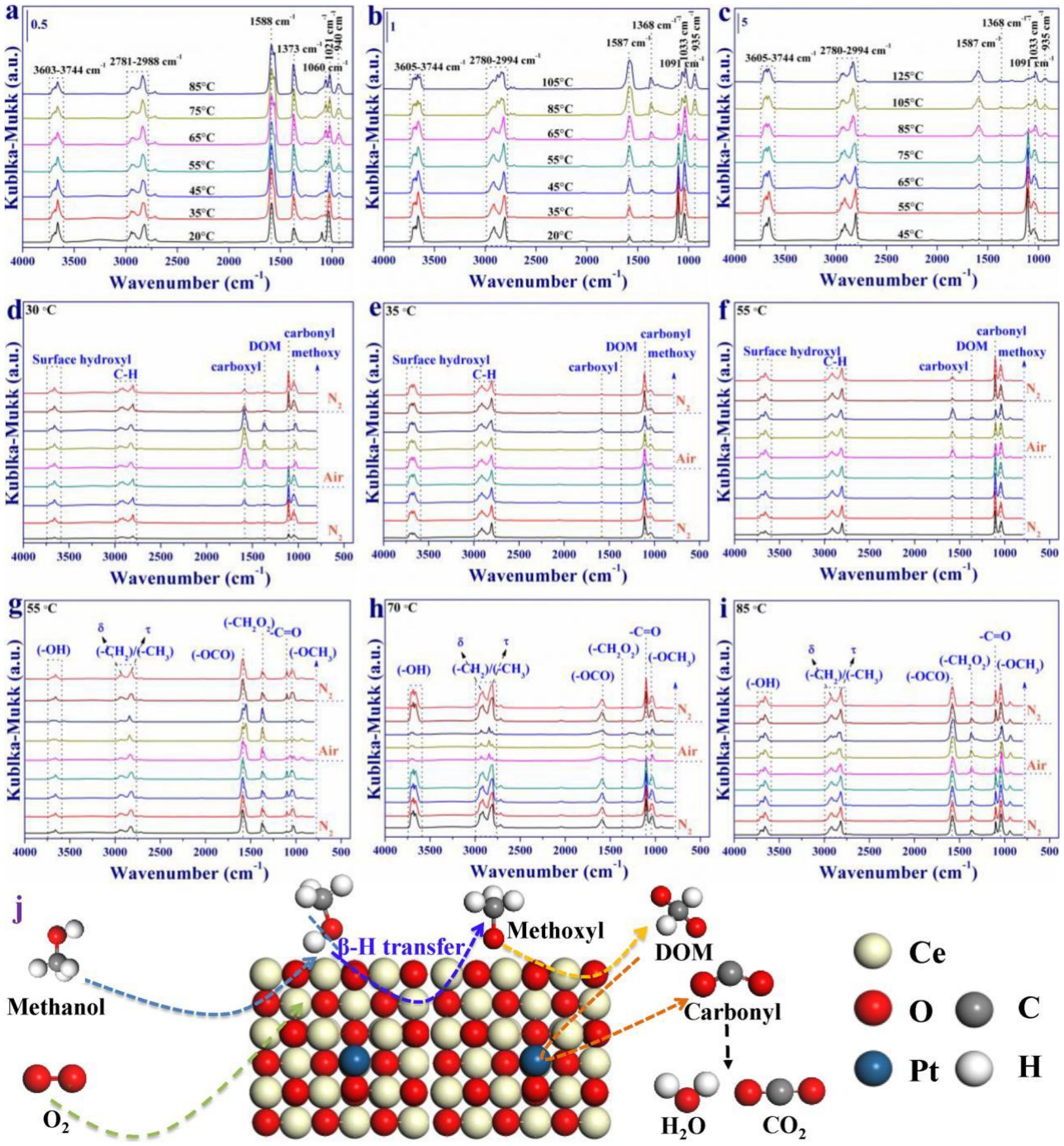

Fig. 8. In situ DRIFTS spectra for methanol oxidation over (a,d,g) Pt_1-CeO_2{100}, (b,e,h) Pt_1-CeO_2{110} and (c,f,i) Pt_1-CeO_2{111} single atom catalysts; (j) The proposed oxidation mechanism for methanol oxidation over Pt_1-CeO_2{100} catalyst.

exothermic reaction energy of 2.99 eV. It takes 0.56 eV to make H_2O desorption (state (f)). Then, the H of CHO_2 transfer to surface O_sH species accompanied by the generation of CO_2 and H_2O (state (g)). The step of $CHO_2 + O_sH \rightarrow CO_2 + H_2O_s$ takes endothermic energy of 1.61 eV. After CO_2 and H_2O desorption (E_{des} =1.59 eV), the surface restores to the Pt_1-distorted-CeO_2(100) surface with one oxygen va-cancy (state (h)).

Surface adsorbed oxygen species can fill in the oxygen vacancy and contributes the surface to restore. The process of surface recovery from one oxygen vacancy surface to the stoichiometric surface on Pt_1-dis-torted-CeO_2(100) catalyst is further investigated and shown in Fig. 10. The vacancy site with E_{ads} of -2.91 eV (Fig. 10a) creates a large attractive force for oxygen molecules. As a result, OeO bond has an increased distance of 1.51 Å (1.21 Å in the gas phase), suggesting the existence of peroxide-type O_2^{2-} species. Then a dissociation of the OeO bond produces two separate oxygen atoms with one connected with Pt atom and the other occupying the oxygen vacancy. The reaction energy of OeO bond cleavage is -2.38 eV and no activation barrier (Fig. 10b). H atoms from the dissociative chemisorption of water can strongly adsorb on the surface oxygen atoms with the exothermic en-ergy of 3.40 (Fig. 10c) and 3.79 eV (Fig. 10d), respectively. Now, the surface is covered with hydroxyl groups. One H can migrate from lattice oxygen to the OH group bonding with the Pt atom to form H_2O (Fig. 10e). This is an endothermic process by 1.81 eV. At last, the

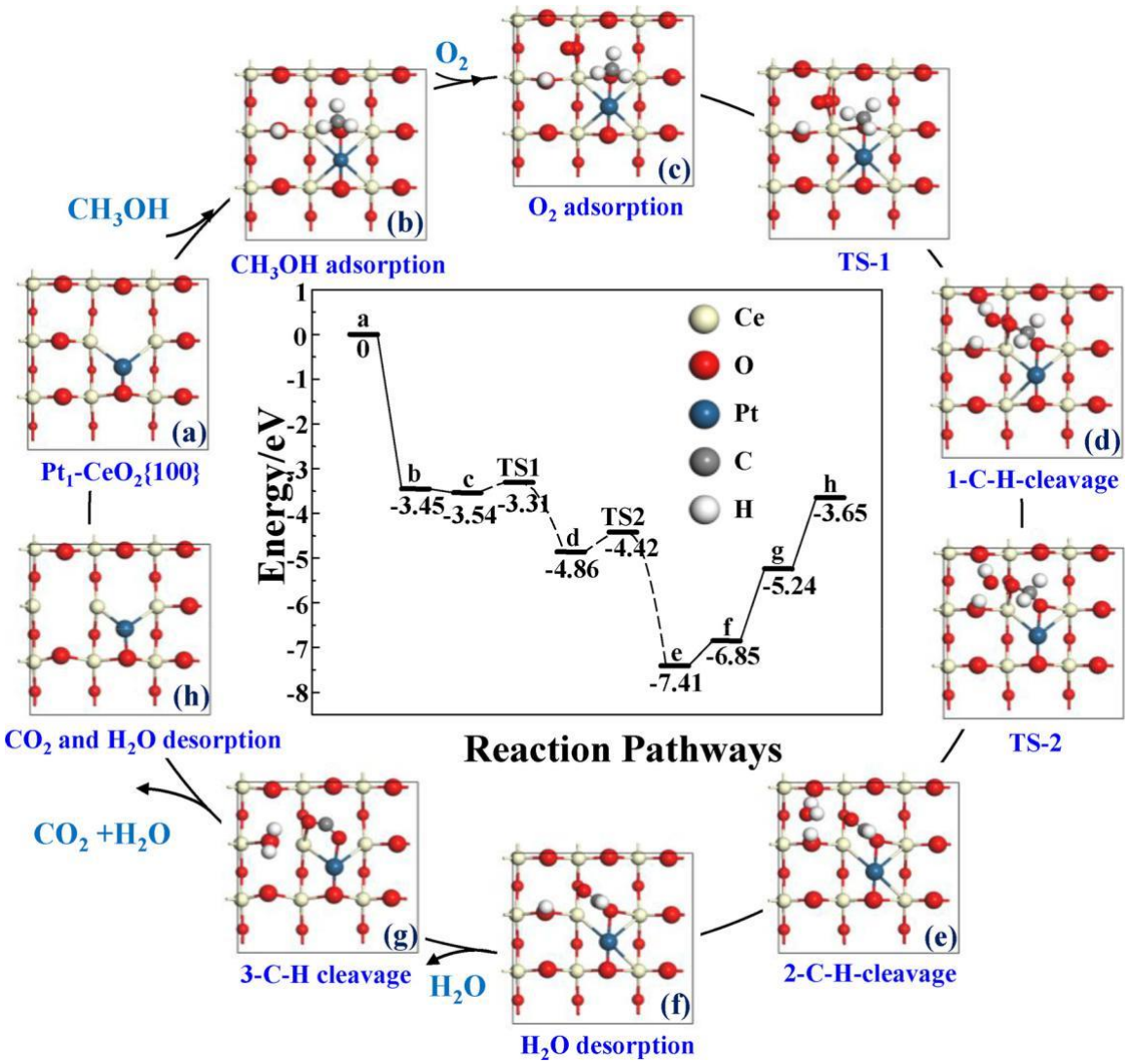

Fig. 9. (a-h) The proposed dynamic mechanism during methanol oxidation over single atom Pt_1-CeO_2{100} material.

surface restores to initial Pt_1-distorted-CeO_2(100) surface after H_2O molecule desorption (Fig. 10f) and this step release an energy of 1.50 eV.

4. Conclusions

In summary, we have attempted to develop the stable single atom materials for thermo-catalytic reactions and made clear the stabilizing mechanism induced by classical strong metal-support interaction. Pt-O-Ce interface was constructed by stabilizing Pt atoms on the surface mono-oxygen vacancies of CeO_2 with diverse exposed facets. Combination of advanced characterizations and theoretical calcula-tions, the stabilization mechanism was creatively proposed that the formed Pt-O-Ce interface will be taken into distortion spontaneously to keep thermodynamics stable through strong metal-support interactions. The distortion of Pt-O-Ce interface balances the Fermi energy level and charge density between Pt species and CeO_2 support, which in turn brings about the variation of valence state and electronic structure of materials. The ratio of Ce^{3+} species is a clear positive correlation with the distortion degree of the interface, which could be expected on condition that this species is known as a pivotal role for stabilization of single atom sites in thermal reactions. Compared with Pt_1-CeO_2{110} and Pt_1-CeO_2{111} samples, the Pt-O-Ce active interface over Pt_1-CeO_2{100} exhibits the highest intensity of distortion degree and thus catalyst possesses the exceptional catalytic efficiency and thermal sta-bility for oxygenated hydrocarbon removal. The enhanced adsorption capacity of O_2 and methanol confirmed in the distortion interface is seen as another crucial reason for improving the stability of SACs. Importantly, the intrinsic methanol oxidation mechanism on prepared single atom material was revealed, over which the methanol activation obeys the L-H mechanism under relative low temperature and then goes through to the MVK mechanism under elevated temperatures. These new findings provide valuable guidance for understanding the stabi-lizing mechanism of SACs through classical strong metal-support in-teraction and propose a versatile platform for facile accessing stable SACs utilized in various industrial thermal reactions.

CRediT authorship contribution statement

Zeyu Jiang: Writing - original draft, Investigation, Formal analysis. Meizan Jing: Writing - original draft, Methodology. Xiangbo Feng: Formal analysis. Jingchao Xiong: Resources. Chi He: Supervision, Project administration, Writing - review & editing, Data curation. Mark Douthwaite: Writing - review & editing. Lirong Zheng: Software, Formal analysis. Weiyu Song: Software, Validation. Jian Liu: Supervision, Software, Validation. Zhiguo Qu: Supervision, Methodology.

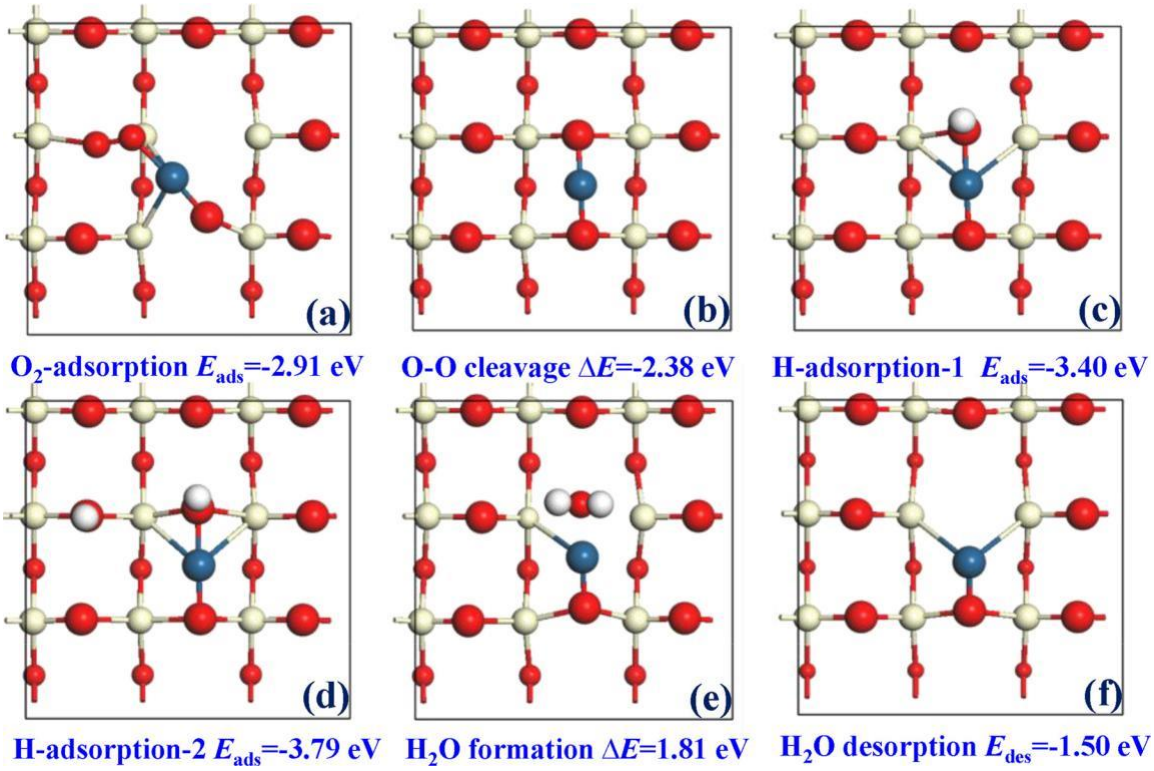

Fig. 10. (a-f) Surface reconstruction process during methanol oxidation over single atom Pt_1-CeO_2{100} material.

Declaration of Competing Interest

The authors declare that they have no known competing financial interests or personal relationships that could have appeared to influ-ence the work reported in this paper.

Acknowledgments

This work was financially supported by the National Natural Science Foundation of China (21876139, 21922606, 21677114), the Key R&D Program of Shaanxi Province (2019SF-244, 2019ZDLSF05-05-02), the Shaanxi Natural Science Fundamental Shaanxi Coal Chemical Joint Fund (2019JLM-14), and Basic Science Center Program for Ordered Energy Conversion of the National Natural Science Foundation of China (51888103). The authors gratefully acknowledge the support of K.C. Wong Education Foundation and also appreciate the editor and re-viewers for their professional work and valuable comments.

Appendix A. Supplementary data

Supplementary material related to this article can be found, in the online version, at doi:https://doi.org/10.1016/j.apcatb.2020.119304.

References

[1] L. Liu, A. Corma, Metal catalysts for heterogeneous catalysis: from single atoms to nanoclusters and nanoparticles, Chem. Rev. 118 (2018) 4981–5079, https://doi.org/10.1021/acs.chemrev.7b00776.
[2] A. Wang, J. Li, T. Zhang, Heterogeneous single-atom catalysis, Nat. Rev. Chem. 2 (2018) 65–81, https://doi.org/10.1038/s41570-018-0010-1.
[3] Y. Chen, S. Ji, C. Chen, Q. Peng, D. Wang, Y. Li, Single-atom catalysts: synthetic strategies and electrochemical applications, Joule 2 (2018) 1242–1264, https://doi.org/10.1016/j.joule.2018.06.019.
[4] X. Su, X.-F. Yang, Y. Huang, B. Liu, T. Zhang, Single-atom catalysis toward efficient CO_2 conversion to CO and formate products, Acc. Chem. Res. 52 (2019) 656–664, https://doi.org/10.1021/acs.accounts.8b00478.
[5] L. Jiao, H. Jiang, Metal-organic-framework-based single-atom catalysts for energy applications, Chem 5 (2019) 786–804, https://doi.org/10.1016/j.joule.2018.06.019.
[6] C. He, Z. Jiang, M. Ma, X. Zhang, M. Douthwaite, J.-W. Shi, Z. Hao, Understanding the promotional effect of Mn_2O_3 on micro-/mesoporous hybrid silica nanocubic-supported Pt catalysts for the low-temperature destruction of methyl ethyl ketone: an experimental and theoretical study, ACS Catal. 8 (2018) 4213–4229, https://doi.org/10.1021/acscatal.7b04461.
[7] M. Tian, X. Guo, R. Dong, Z. Guo, J. Shi, Y. Yu, M. Chen, R. Albilali, C. He, Insight into the boosted catalytic performance and chlorine resistance of nanosphere-like meso-macroporous CrO_x/$MnCo_3O_x$ for 1,2-dichloroethane destruction, Appl. Catal. B: Environ. 259 (2019) 118018, https://doi.org/10.1016/j.apcatb.2019.118018.
[8] C. He, J. Cheng, X. Zhang, M. Douthwaite, S. Pattisson, Z. Hao, Recent advances in the catalytic oxidation of volatile organic compounds: a review based on pollutant sorts and sources, Chem. Rev. 119 (2019) 4471–4568, https://doi.org/10.1021/acs.chemrev.8b00408.
[9] H. Huang, C. Chen, R. Yang, Y. Yu, R. Albilali, C. He, Remarkable promotion effect of lauric acid on Mn-MIL-100 for non-thermal plasma-catalytic decomposition of toluene, Appl. Surf. Sci. 503 (2020) 144290, https://doi.org/10.1016/j.apsusc. 2019.144290.
[10] K. Yang, Y. Liu, J. Deng, X. Zhao, J. Yang, Z. Han, Z. Huo, H. Dai, Three-di-mensionally ordered mesoporous iron oxide-supported single-atom platinum: highly active catalysts for benzene combustion, Appl. Catal. B: Environ. 244 (2019) 650–659, https://doi.org/10.1016/j.apcatb.2018.11.077.
[11] P. Hu, Z. Huang, Z. Amghouz, M. Makkee, F. Xu, F. Kapteijn, A. Dikhtiarenko, Y. Chen, X. Gu, X. Tang, Electronic metal-support interactions in single-atom cat-alysts, Angew. Chem. Int. Ed. 53 (2014) 3418–3421, https://doi.org/10.1002/ange. 201309248.
[12] Z. Jiang, X. Feng, J. Deng, C. He, M. Douthwaite, Y. Yu, J. Liu, Z. Hao, Z. Zhao, Atomic-scale insights into the low-temperature oxidation of methanol over a single-atom Pt_1-Co_3O_4 catalyst, Adv. Funct. Mater. (2019) 1902041, https://doi.org/10.1002/adfm.201902041.
[13] H. Li, M. Wang, L. Luo, J. Zeng, Static regulation and dynamic evolution of single-atom catalysts in thermal catalytic reactions, Adv. Sci. 6 (2019) 1801471, https://doi.org/10.1002/advs.201801471.
[14] L. Nie, D. Mei, H. Xiong, B. Peng, Z. Ren, X. Hernandez, A. DeLaRiva, M. Wang, M. Engelhard, L. Kovarik, A. Datye, Y. Wang, Activation of surface lattice oxygen in single-atom Pt/CeO_2 for low-temperature CO oxidation, Science 358 (2017) 1419–1423, https://doi.org/10.1126/science.aao2109.
[15] R. Qin, P. Liu, G. Fu, N. Zheng, Strategies for stabilizing atomically dispersed metal catalysts, Small Methods (2017) 1700286, https://doi.org/10.1002/smtd. 201700286.
[16] J. Jones, H. Xiong, A. DeLaRiva, E. Peterson, H. Pham, S. Challa, G. Qi, S. Oh, M. Wiebenga, X. Hernández, Y. Wang, A. Datye, Thermally stable single-atom Platinum-on-ceria catalysts via atom trapping, Science 353 (2016) 150–154, https://doi.org/10.1126/science.aaf8800.
[17] R. Lang, W. Xi, J.-C. Liu, Y. Cui, T. Li, A. Lee, F. Chen, Y. Chen, L. Li, L. Li, J. Lin, S. Miao, X. Liu, A.-Q. Wang, X. Wang, J. Luo, B. Qiao, J. Li, T. Zhang, Non defect-

stabilized thermally stable single-atom catalyst, Nat. Commun. 10 (2019) 234, https://doi.org/10.1038/s41467-018-08136-3.
[18] M. Hülsey, J. Zhang, N. Yan, Harnessing the wisdom in colloidal chemistry to make stable single-atom catalysts, Adv. Mater. 30 (2018) 1802304, https://doi.org/10.1002/adma.201802304.
[19] L. Wang, L. Wang, X. Meng, F.-S. Xiao, New strategies for the preparation of sinter-resistant metal-nanoparticle-based catalysts, Adv. Mater. (2019) 1901905, https://doi.org/10.1002/adma.201901905.
[20] W. Zhan, Q. He, X. Liu, Y. Guo, Y. Wang, L. Wang, Y. Guo, A. Borisevich, J. Zhang, G. Lu, S. Dai, A sacrificial coating strategy toward enhancement of metal-support interaction for ultrastable Au nanocatalysts, J. Am. Chem. Soc. 138 (2016) 16130–16139, https://doi.org/10.1021/jacs.6b10472.
[21] L. DeRita, S. Dai, K. Lopez-Zepeda, N. Pham, G. Graham, X. Pan, P. Christopher, Catalyst architecture for stable single atom dispersion enables site specific spectroscopic and reactivity measurements of CO adsorbed to Pt atoms, oxidized Pt clusters, and metallic Pt clusters on TiO_2, J. Am. Chem. Soc. 139 (2017) 14150–14165, https://doi.org/10.1021/jacs.7b07093.
[22] J. Zhang, H. Wang, L. Wang, S. Ali, C. Wang, L. Wang, X. Meng, B. Li, D. Su, F.-S. Xiao, Wet-chemistry strong metal-support interactions in titania supported Au catalysts, J. Am. Chem. Soc. 141 (2019) 2975–2983, https://doi.org/10.1021/jacs.8b10864.
[23] Y. Tang, S. Zhao, B. Long, J.-C. Liu, J. Li, On the nature of support effects of metal dioxides MO_2 (M = Ti, Zr, Hf, Ce, Th) in single-atom gold catalysts: importance of quantum primogenic effect, J. Phys. Chem. C 120 (2016) 17514–17526, https://doi.org/10.1021/acs.jpcc.6b05338.
[24] N. O`Connor, A. Jonayat, M. Janik, T. Senftle, Interaction trends between single metal atoms and oxide supports identified with density functional theory and sta-tistical learning, Nat. Catal. 1 (2018) 531–539, https://doi.org/10.1038/s41929-018-0094-5.
[25] A. Therrien, A. Hensley, M. Marcinkowski, R. Zhang, F. Lucci, B. Coughlin, A. Schilling, J.-S. McEwen, E. Sykes, An atomic-scale view of single-site Pt catalysis for low-temperature CO oxidation, Nat. Catal. 1 (2018) 192–198, https://doi.org/10.1038/s41929-018-0028-2.
[26] Z. Wang, Z. Huang, J. Brosnahan, S. Zhang, Y. Guo, Y. Guo, L. Wang, Y. Wang, W. Zhan, Ru/CeO_2 catalyst with optimized CeO_2 support morphology and surface facets for propane combustion, Environ. Sci. Technol. 53 (2019) 5349–5358, https://doi.org/10.1021/acs.est.9b01929.
[27] C. Sun, H. Li, L. Chen, Nanostructured ceria-based materials: synthesis, properties, and applications, Energy Environ. Sci. 5 (2012) 8475–8505, https://doi.org/10.1039/C2EE22310D.
[28] A. LaGrow, M. Ward, D. Lloyd, P. Gai, E. Boyes, Visualizing the Cu/Cu_2O interface transition in nanoparticles with environmental scanning transmission electron microscopy, J. Am. Chem. Soc. 139 (2017) 179–185, https://doi.org/10.1021/jacs.6b08842.
[29] D. Gao, Y. Zhang, Z. Zhou, F. Cai, X. Zhao, W. Huang, Y. Li, J. Zhu, P. Liu, F. Yang, G. Wang, X. Bao, Enhancing CO_2 electroreduction with the metal-oxide interface, J. Am. Chem. Soc. 139 (2017) 5652–5655, https://doi.org/10.1021/jacs.7b00102.
[30] M. Cargnello, V. Doan-Nguyen, T. Gordon, R. Diaz, E. Stach, E. Stach, R. Gorte, P. Fornasiero, C. Murray, Control of metal nanocrystal size reveals metal-support interface role for ceria catalysts, Science 341 (2013) 771–773, https://doi.org/10.1126/science.1240148.
[31] N. Ta, J. Liu, S. Chenna, P. Crozier, Y. Li, A. Chen, W. Shen, Stabilized gold nanoparticles on ceria nanorods by strong interfacial anchoring, J. Am. Chem. Soc. 134 (2012) 20585–20588 https://doi.org/10.1021/ja310341j.
[32] X. Liu, K. Zhou, L. Wang, B. Wang, Y. Li, Oxygen vacancy clusters promoting reducibility and activity of ceria nanorods, J. Am. Chem. Soc. 131 (2009) 3140–3141 https://doi.org/10.1021/ja808433d.
[33] G. Kresse, J. Furthmuller, Efficient iterative schemes for ab initio total-energy calculations using a plane-wave basis set, Phys. Rev. B 54 (1996) 11169–11186, https://doi.org/10.1103/physrevb.54.11169.
[34] J. Perdew, K. Burke, M. Ernzerhof, Generalized gradient approximation made simple, Phys. Rev. Lett. 77 (1996) 3865, https://doi.org/10.1103/physrevlett.77. 3865.
[35] P. Blöchl, Projector augmented-wave method, Phys. Rev. B 50 (1994) 17953–17979, https://doi.org/10.1103/PhysRevB.50.17953.
[36] M. Cococcioni, S. Gironcoli, Linear response approach to the calculation of the ef-fective interaction parameters in the LDA+U method, Phys. Rev. B 71 (2005) 035105, , https://doi.org/10.1103/PhysRevB.71.035105.
[37] M. Jing, W. Song, L. Chen, S. Ma, J. Deng, H. Zheng, Y. Li, J. Liu, Z. Zhao, Density functional theory study of the formaldehyde catalytic oxidation mechanism on a Au-doped CeO_2(111) surface, J. Phys. Chem. C 122 (2018) 438–448, https://doi.org/10.1021/acs.jpcc.7b09276.
[38] Y. Tang, Y. Wang, J. Li, Theoretical investigations of Pt_1@CeO_2 single-atom catalyst for CO oxidation, J. Phys. Chem. C 121 (2017) 11281–11289, https://doi.org/10.1021/acs.jpcc.7b00313.
[39] M. Capdevila-Cortada, M. García-Melchor, N. López, Unraveling the structure sensitivity in methanol conversion on CeO_2: a DFT + U study, J. Catal. 327 (2015) 58–64, https://doi.org/10.1016/j.jcat.2015.04.016.
[40] G. Henkelman, H. Jónsson, A climbing image nudged elastic band method for finding saddle points and minimum energy paths, J. Chem. Phys. 113 (2000) 9901–9904, https://doi.org/10.1063/1.1329672.
[41] W. Wang, C. Li, X. Zhang, M. Wei, D. Evans, X. Duan, Catalytic behavior of sup-ported Ru nanoparticles on the {100}, {110}, and {111} facet of CeO_2, J. Catal. 329 (2015) 177–186, https://doi.org/10.1016/j.jcat.2015.05.014.
[42] R. Si, M. Flytzani-Stephanopoulos, Shape and crystal-plane effects of nanoscale ceria on the activity of Au-CeO_2 catalysts for the water-gas shift reaction, Angew. Chem. Int. Ed. 47 (2008) 2884–2887, https://doi.org/10.1002/anie.200705828.
[43] F. Esch, S. Fabris, L. Zhou, T. Montini, C. Africh, P. Fornasiero, G. Comelli, R. Rosei, Electron localization determines defect formation on ceria substrates, Science 309 (2005) 752–755, https://doi.org/10.1126/science.1111568.
[44] K. Ding, A. Gulec, A. Johnson, N. Schweitizer, G. Stucky, L. Mark, P. Stair, Identification of active sites in CO oxidation and water-gas shift over supported Pt catalysts, Science 350 (2015) 189–192, https://doi.org/10.1126/science.aac6368.
[45] H. Thang, G. Pacchioni, L. DeRita, P. Christopher, Nature of stable single atom Pt catalysts dispersed on anatase TiO_2, J. Catal. 367 (2018) 104–114, https://doi.org/10.1016/j.jcat.2018.08.025.
[46] Y. Qu, B. Chen, Z. Li, X. Duan, L. Wang, Y. Lin, T. Yuan, F. Zhou, Y. Hu, Z. Yang, C. Zhao, J. Wang, C. Zhao, Y. Hu, G. Wu, Q. Zhang, Q. Xu, B. Liu, P. Gao, R. You, W. Huang, L. Zheng, L. Gu, Y. Wu, Y. Li, Thermal emitting strategy to synthesize atomically dispersed Pt metal sites from bulk Pt metal, J. Am. Chem. Soc. 141 (2019) 4505–4509, https://doi.org/10.1021/jacs.8b09834.
[47] C. Dessal, A. Sangnier, C. Chizallet, C. Dujardin, F. Morfin, J.-L. Rousset, M. Aouine, M. Bugnet, P. Afanasiev, L. Piccolo, Atmosphere-dependent stability and mobility of catalytic Pt single atoms and clusters on γ-Al_2O_3, Nanoscale 11 (2019) 6897–6904, https://doi.org/10.1039/C9NR01641D.
[48] Y. Liu, Z. Li, Q. Yu, Y. Chen, Z. Chai, G. Zhao, S. Liu, W.-C. Cheong, Y. Pan, Q. Zhang, L. Gu, L. Zheng, Y. Wang, Y. Lu, D. Wang, C. Chen, Q. Peng, Y. Liu, L. Liu, J. Chen, Y. Li, A general strategy for fabricating isolated single metal atomic site catalysts in Y zeolite, J. Am. Chem. Soc. 141 (2019) 9305–9311, https://doi.org/10.1021/jacs.9b02936.
[49] S. Lee, S. Lee, D. Gerceker, M.D. Kumbhalkar, K.M. Wiaderek, M.R. Ball, M. Mavrikakis, J.A. Dumesic, R.E. Winans, In situ, operando studies on the size and structure of supported Pt catalysts under supercritical conditions by simultaneous synchrotron-based X-ray techniques, Phys. Chem. Chem. Phys. 21 (2019) 11740–11747, https://doi.org/10.1039/C9CP00347A.
[50] Z. Zhang, Y. Chen, L. Zhou, C. Chen, Z. Han, B. Zhang, Q. Wu, L. Yang, L. Du, Y. Bu, P. Wang, X. Wang, H. Yang, H. Zheng, The simplest construction of single-site catalysts by the synergism of micropore trapping and nitrogen anchoring, Nat. Commun. 10 (2019) 1657, https://doi.org/10.1038/s41467-019-09596-x.
[51] A.M. Shahin, F. Grandjean, G.J. Long, T.P. Schuman, Cerium L_{III}-edge XAS investigation of the structure of crystalline and amorphous cerium oxides, Chem. Mater. 17 (2005) 315–321, https://doi.org/10.1021/cm0492437.
[52] P. Bera, K.R. Priolkar, A. Gayen, P.R. Sarode, M.S. Hedge, S. Emura, R. Kumashiro, V. Jayaram, G.N. Subbana, Ionic dispersion of Pt over CeO_2 by the combustion method: structural investigation by XRD, TEM, XPS, and EXAFS, Chem. Mater. 15 (2003) 2049–2060, https://doi.org/10.1021/cm0204775.
[53] B. Kossoy, A. Frenkel, Q. Wang, E. Wachtel, I. Lubomirsky, Local structure and strain-induced distortion in $Ce_{0.8}Gd_{0.2}O_{1.9}$, Adv. Mater. 22 (2010) 1659–1662, https://doi.org/10.1002/adma.200902041.
[54] Y. Ogura, K. Sato, S.-I. Miyahara, Y. Kawano, T. Toriyama, T. Yamamoto, S. Matsumura, S. Hosokawa, K. Nagaoka, Efficient ammonia synthesis over a Ru/$La_{0.5}Ce_{0.5}O_{1.75}$ catalyst pre-reduced at high temperature, Chem. Sci. 9 (2018) 2230–2237, https://doi.org/10.1039/c7sc05343f.
[55] X. Hao, A. Yoko, C. Chen, K. Inoue, M. Saito, G. Seong, S. Takami, T. Adschiri, Y. Ikuhara, Atomic-scale valence state distribution inside ultrafine CeO_2 nanocubes and its size dependence, Small 14 (2018) 1802915, https://doi.org/10.1002/smll. 201802915.
[56] S. Zhang, Z.-Q. Huang, Y. Ma, W. Guo, J. Li, F. Cao, L. Li, C.-R. Chang, Y. Qu, Solid frustrated-lewis-pair catalysts constructed by regulations on surface defects of porous nanorods of CeO_2, Nat. Commun. 8 (2017) 15266, https://doi.org/10.1038/ncomms15266.
[57] Q. Zhu, Z. Jiang, M. Ma, C. He, Y. Yu, X. Liu, R. Albilali, Revealing the unexpected promotion effect of diverse potassium precursors on α-MnO_2 for the catalytic de-struction of toluene, Catal. Sci. Technol. 10 (2020) 2100–2110, https://doi.org/10.1039/c9cy02347j.
[58] R. Si, Y.-W. Zhang, L.-P. You, C.-H. Yan, Rare-earth oxide nanopolyhedra, nanoplates, and nanodisks, Angew. Chem. Int. Ed. 44 (2005) 3256–3260, https://doi.org/10.1002/anie.200462573.
[59] M. Guo, J. Lu, Y. Wu, Y. Wang, M. Luo, UV and visible raman studies of oxygen vacancies in rare-earth-doped ceria, Langmuir 27 (2011) 3872–3877, https://doi.org/10.1021/la200292f.
[60] V. Araújo, W. Avansi, H. Carvalho, M. Moreira, E. Longo, C. Ribeiro, M. Bernardi, CeO_2 nanoparticles synthesized by a microwave-assisted hydrothermal method: evolution from nanospheres to nanorods, CrystEngComm 14 (2012) 1150–1154, https://doi.org/10.1039/C1CE06188G.
[61] W. Wang, Q. Zhu, F. Qin, Q. Dai, X. Wang, Fe Doped CeO_2 nanosheets as fenton-like heterogeneous catalysts for degradation of salicylic acid, Chem. Eng. J. 333 (2018) 226–239, https://doi.org/10.1016/j.cej.2017.08.065.
[62] A. Tamilselvan, S. Balakumar, M. Sakar, Chiranjib Nayek, P. Murugavel, K. Saravana Kumar, Role of oxygen vacancy and Fe-O-Fe bond angle in composi-tional, magnetic, and dielectric relaxation on Eu-substituted $BiFeO_3$ nanoparticles, Dalton Trans. 43 (2014) 5731–5738, https://doi.org/10.1039/C3DT52260A.
[63] X. Feng, C. Chen, C. He, S. Chai, Y. Yu, J. Cheng, Non-thermal plasma coupled with MOF-74 derived Mn-Co-Ni-O porous composite oxide for toluene efficient de-gradation, J. Hazard. Mater. 383 (2020) 121143, https://doi.org/10.1016/j. jhazmat.2019.121143.
[64] T. Yan, W. Dai, G. Wu, S. Lang, M. Hunger, N. Guan, L. Li, Mechanistic insights into one-step catalytic conversion of ethanol to butadiene over bifunctional Zn-Y/Beta zeolite, ACS Catal. 8 (2018) 2760–2773, https://doi.org/10.1021/acscatal.8b00014.
[65] V. Veena, K. Illath, A. Lazar, C. Vinod, T. Ajithkumar, S. Javanthi, Distribution of water in the pores of periodic mesoporous organosilicates-a proton solid state MAS

NMR study, Phys. Chem. Chem. Phys. 20 (2018) 29351–29361, https://doi.org/10.1039/C8CP04902E.
[66] S. Kattel, B. Yan, Y. Yang, J. Chen, P. Liu, Optimizing binding energies of key intermediates for CO_2 hydrogenation to methanol over oxide-supported copper, J. Am. Chem. Soc. 138 (2016) 12440–12450, https://doi.org/10.1021/jacs.6b05791.
[67] T. Tan, J. Scott, Y. Ng, R. Taylor, K.-F. Aguey-Zinsou, R. Amal, C-C sleavage by Au/TiO_2 during ethanol oxidation: understanding band gap photoexcitation and plasmonically mediated charge transfer via quantitative in situ DRIFTS, ACS Catal. 6 (2016) 8021–8029, https://doi.org/10.1021/acscatal.6b01833.
[68] J. Guo, C. Lin, C. Jiang, P. Zhang, Review on noble metal-based catalysts for formaldehyde oxidation at room temperature, Appl. Surf. Sci. 475 (2019) 237–255, https://doi.org/10.1016/j.apsusc.2018.12.238.
[69] J. Wang, P. Zhang, J. Li, C. Jiang, R. Yunus, J. Kim, Room-temperature oxidation of formaldehyde by layered manganese oxide: effect of water, Environ. Sci. Technol. 49 (2015) 12372–12379, https://doi.org/10.1021/acs.est.5b02085.